Seismicity on a fault controlled by rate- and state-dependent friction with spatial variations of the critical slip distance

G. Hillers
Institute of Geophysics, ETH Hoenggerberg, Zürich, Switzerland

Y. Ben-Zion
Department of Earth Sciences, University of Southern California, Los Angeles, California, USA

P. M. Mai
Institute of Geophysics, ETH Hoenggerberg, Zürich, Switzerland

Received 2 June 2005; revised 12 September 2005; accepted 19 October 2005; published 21 January 2006.

[1] We perform systematic simulations of slip using a quasi-dynamic continuum model of a two-dimensional (2-D) strike-slip fault governed by rate- and state-dependent friction. The depth dependence of the $a - b$ and L frictional parameters are treated in an innovative way that is consistent with available laboratory data and multidisciplinary field observations. Various realizations of heterogeneous L distributions are used to study effects of structural variations of fault zones on spatiotemporal evolution of slip. We demonstrate that such realizations can produce within the continuum class of models realistic features of seismicity and slip distributions on a fault. We explore effects of three types of variable L distributions: (1) a depth-dependent L profile accounting for the variable width of fault zones with depth, (2) uncorrelated 2-D random distributions of L with different degrees of heterogeneity, and (3) a hybrid distribution combining the depth-dependent L profile with the 2-D random L distributions. The first type of L distribution, with relatively small L over the depth range corresponding to the seismogenic zone and larger L elsewhere, generates stick-slip events in the seismogenic zone and ongoing creep above and below that region. The 2-D heterogeneous parameterizations generate frequency-size statistics with event sizes spanning 4 orders of magnitude. Our results indicate that different degrees of heterogeneity of L distributions control (1) the number of simulated events and (2) the overall stress level and fluctuations. Other observable trends are (3) the dependency of hypocenter location on L and (4) different nucleation phases for small and large events in heterogeneous distributions.

Citation: Hillers, G., Y. Ben-Zion, and P. M. Mai (2006), Seismicity on a fault controlled by rate- and state-dependent friction with spatial variations of the critical slip distance, *J. Geophys. Res.*, *111*, B01403, doi:10.1029/2005JB003859.

1. Introduction

[2] In the past three decades, rate- and state-dependent (RS) friction laws have been successfully applied to numerous aspects of earthquake and fault mechanics [e.g., *Dieterich*, 1979; *Ruina*, 1983; *Scholz*, 2002]. Being originally derived to fit laboratory data of frictional experiments, the empirical RS friction was shown to be a powerful tool in modeling various stages of the seismic cycle. The RS formulation combines the logarithmic increase of static friction with hold time and the slip weakening behavior during dynamic instabilities in a unified and consistent manner. Rate- and state-dependent friction laws were applied in one-dimensional (1-D), 2-D, and 3-D fault models to simulate seismic cycles including preseismic slip and nucleation, the growth of dynamic instabilities, healing of fault surfaces, earthquake afterslip, aftershocks, and long deformation histories [*Tse and Rice*, 1986; *Rice*, 1993; *Dieterich*, 1994; *Ben-Zion and Rice*, 1995; *Marone*, 1998]. RS friction has also been used to describe variations of seismicity rates and related changes of earthquake patterns [*Dieterich et al.*, 2000; *Parsons et al.*, 2000; *Toda et al.*, 2002; *Stein*, 2003].

[3] Previous studies of spatiotemporal evolution of slip on a fault governed by rate- and state-dependent friction [e.g., *Rice*, 1993; *Ben-Zion and Rice*, 1997; *Tullis*, 1996; *Lapusta et al.*, 2000] employed frictional properties corresponding to fairly homogeneous faults. In most cases, the only types of heterogeneities were lab-based depth variations of the parameters a and b that produce transitions between stable velocity-strengthening ($a > b$) and unstable velocity-weakening regimes ($a < b$) (Figure 1).

0148-0227/06/2005JB003859$09.00

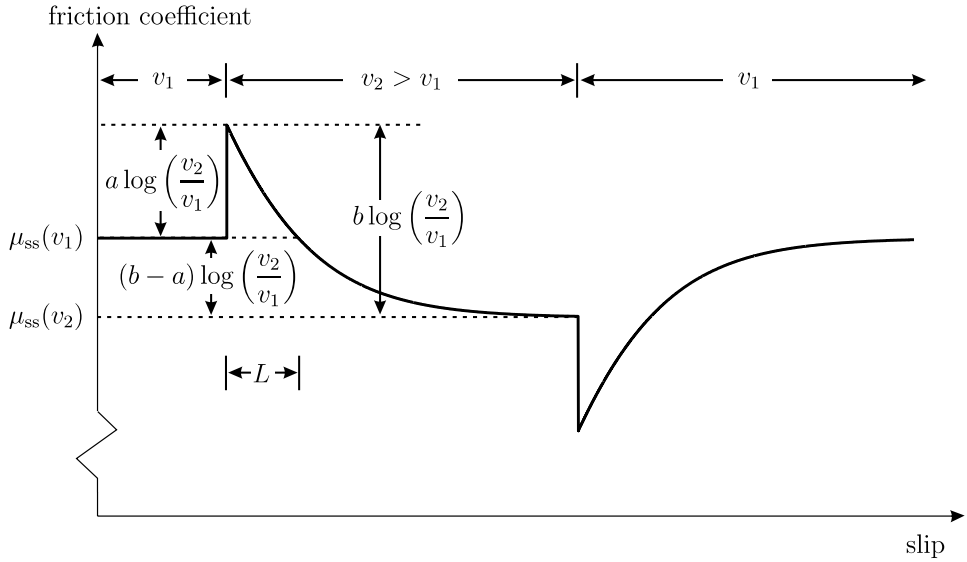

Figure 1. Schematic diagram summarizing the main features of rate- and state-dependent friction obtained in laboratory experiments with slip rates in the range of 10^{-6}–5×10^{-4} m/s. Constitutive parameters a and b relate changes in slip rate ($v_1 \rightarrow v_2 > v_1$) and state to frictional strength. L is the slip distance for evolution of the friction coefficient μ.

[4] In velocity stepping experiments, a and b are constitutive parameters relating changes in slip rate and state to frictional strength. The parameter a characterizes the increase in strength with accelerated slip, and b reflects the increase in strength with increasing total area. The onset of creep due to temperature-induced quartz plasticity explains the velocity-strengthening regime below ~15 km depth in the commonly used $a - b$ profile obtained from data collected by *Blanpied et al.* [1991]. However, the physical origin of the transition at ~3 km depth is less constrained. Synoptic models of shear zones [e.g., *Scholz*, 1988] suggest a stable $a > b$ regime for the topmost portion of faults due to highly fractured and less consolidated material that is prone to dilatancy hardening. However, the stabilizing mechanism is not supported unequivocally by data points in the studies of *Blanpied et al.* [1991] and *Stesky* [1975].

[5] Another important frictional parameter is the critical slip distance L for evolution of the friction coefficient (Figure 1). Laboratory measurements show that the critical slip distance L is correlated with the width of the gouge zone [*Marone*, 1998, and references therein], and scales with the dominant wavelength that characterizes the roughness of the sliding surfaces [*Ohnaka*, 2003, and references therein]. This observation is supported by *Perfettini and Campillo* [2003], who concluded that L depends on the observation scale, explaining the discrepancy between laboratory and seismological observations of the characteristic length. A wide range of field observations indicates that the width of the gouge zone in the brittle crust decreases with depth [*Sylvester*, 1988; *Chester and Chester*, 1998; *Ben-Zion et al.*, 2003b] and that fault surfaces become progressively smoother with cumulative slip [*Wesnousky*, 1988; *Stirling et al.*, 1996; *Ben-Zion and Sammis*, 2003]. While natural fault surfaces are not perfectly planar, previous studies have shown that model simulations of heterogeneous faults with planar representations can reproduce the general observed features of earthquake patterns [*Ben-Zion*, 1996; *Miller et al.*, 1999; *Zöller et al.*, 2005b]. Such planar representations are computationally far more efficient than representations that include geometrically complex structures [*Robinson and Benites*, 1995; *Lyakhovsky et al.*, 2001]. It is therefore important to develop improved planar representations that account for observed properties of sliding surfaces.

[6] Previous simulations of earthquakes with planar representations generally fall into continuum models that are independent of the employed grid size [*Rice*, 1993; *Lapusta et al.*, 2000] and inherently discrete models that are grid-size-dependent [*Carlson and Langer*, 1989a; *Ben-Zion and Rice*, 1993; *Zöller et al.*, 2005c]. In this study we use heterogeneities of L along strike and with depth to investigate the effects of geometrical heterogeneities of faults on various aspects of earthquakes within the continuum framework. More specifically, we perform 3-D quasi-dynamic simulations of slip on a vertical strike-slip fault embedded in a 3-D elastic continuum using a family of 2-D anisotropic distributions of L. Applied variations of L along strike may be used to provide approximate representations of faults at different evolutionary stages, whereas variations with depth reflect generalized shear zone architecture. The transition of behavior in the top few kilometers of the crust that was modeled in previous works by depth variations of $a - b$ is accounted for here by depth variations of L. Earthquake catalogs are extracted from the continuous simulated slip histories using a procedure that approximates the quantities derived from observed seismograms. The efficient new design of the present study, treating geometrical heterogeneities of fault zones as geometrical variations of frictional properties in a continuum planar model bridges the gap between the existing discrete and continuous models [*Ben-Zion and Rice*, 1995; *Rice and Ben-Zion*, 1996].

[7] The remainder of the article is organized as follows. In section 2 we provide background material on the formulation problem, the constitutive equations, and their translation into the numerical scheme. In section 3 we discuss

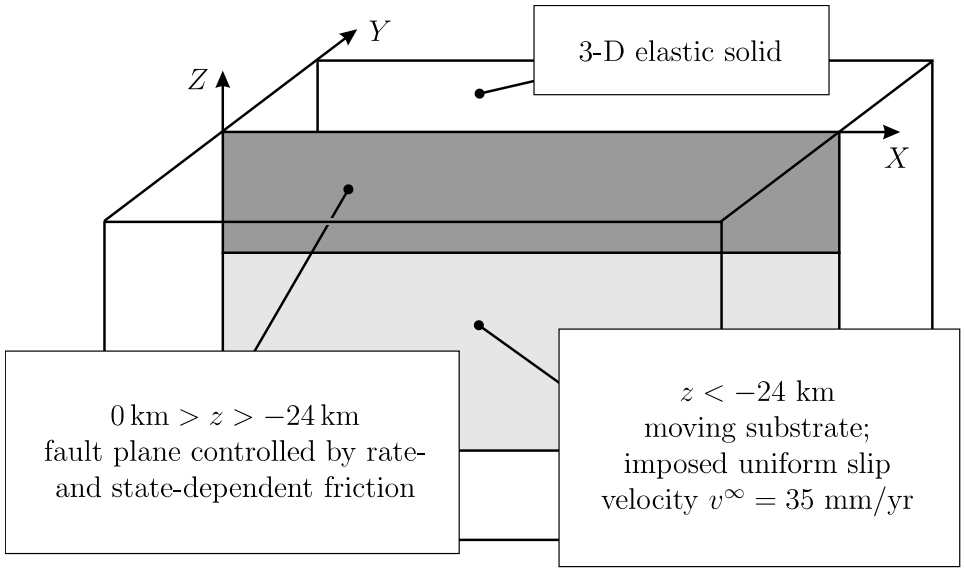

Figure 2. Rate- and state-controlled vertical strike-slip fault plane embedded in a 3-D elastic half-space, loaded by aseismic slip rate v^{∞} = 35 mm/yr at its downward extension. Frictional properties apply over a depth range of 24 km along a fault of length 100 or 200 km.

some basic parameter choices and their influence on the continuum limit approach. Section 4 discusses the response of a standard model to demonstrate the validity of our numerical procedure. We then explore systematically the effects of various depth-dependent L profiles with homogeneous along-strike distributions. In section 5 we introduce a typical implementation example, focusing on the consequences of different $L_{\max}$ values. We proceed with the discussion of seismicity generated by several 2-D distributions with different degrees of heterogeneity approximating fault zones at different evolutionary stages. Finally, in section 6 we present results obtained by a hybrid approach, employing realistic depth-dependent L profiles superposed on heterogeneous L patterns along strike and with depth.

2. Numerical Model

2.1. Stress-Slip Relation

[8] Figure 2 shows the model geometry and coordinate system of a vertical strike-slip fault plane in a 3-D elastic medium of rigidity G and shear wave velocity v_s, following *Rice* [1993], *Ben-Zion and Rice* [1995], *Ben-Zion and Rice* [1997], and *Lapusta et al.* [2000]. The evolution of slip $u(x, z, t)$ on the fault plane $y = 0$ is associated with a redistribution of shear stress $\tau(x, z, t)$. In the discretized case, the resulting integral relation connecting u and τ can be expressed by a set of linear equations based on the quasi-static elastic solution for uniform slip over a rectangular dislocation cell in an elastic half-space [*Chinnery*, 1963]:

$$\tau_{ij}(t) = \tau^0 + \tau^{\mathrm{r}}_{ij}(t) - v_{ij}(t)\,\eta_0. \tag{1}$$

Here, τ^0 is a background stress value chosen to keep $\tau_{ij} > 0$ in cases where slip is possibly overshooting, but τ^0 has no influence on the evolution of the system. Shear stress redistribution due to loading and slip on the fault is given by $\tau^{\mathrm{r}}_{ij}(t) = \sum_k \sum_l K_{|i-k|,j,l}\,(v^{\infty}\,t - u_{kl}(t))$. Indices i, k and j, l denote cell locations on the numerical grid along strike and depth, respectively. The elastostatic kernel (or stiffness matrix) K relates the slip at cell kl, u_{kl}, to change of stress at cell ij, τ_{ij}, at some time t, and was calculated assuming 10 periodic repetitions of the fault along strike to approximate infinite periodic boundary conditions. A constant driving plate velocity, v^{∞}, is imposed at the downward extension of the fault, and $\dot{u}_{ij}(t) = v_{ij}(t)$ is the slip rate of a certain cell. The term η_0 in equation (1) accounts for seismic radiation damping and is equal to $G/(2v_s)$ [*Rice*, 1993]. Including this factor makes the description quasi-dynamic, since it incorporates the elastodynamic limit result for any instantaneous changes in $\tau_{ij}(t)$ and $v_{ij}(t)$. It also has the advantage of allowing stable calculations to be carried through dynamic instabilities, without requiring the computationally expensive calculations of the exact elastodynamic solution performed by *Ben-Zion and Rice* [1997], *Lapusta et al.* [2000], and *Lapusta and Rice* [2003].

2.2. Friction

[9] To describe the frictional resistance between two adjacent fault walls, we use the laboratory derived rate- and state-dependent friction formulation. We apply the standard Dieterich-Ruina description of the friction coefficient, $\mu(x, z, t)$ [*Dieterich*, 1979; *Ruina*, 1983; *Dieterich*, 1994], which depends on sliding velocity, $v(x, z, t)$, and a state variable, $\theta(x, z, t)$,

$$\mu(x,z,t) = \mu_0 + a(z)\,\ln\left(\frac{v(x,z,t)}{v_0}\right) + b(z)\,\ln\left(\frac{v_0\,\theta(x,z,t)}{L(x,z)}\right). \tag{2}$$

The state variable is interpreted as being a measure of maturity of contacts on a fault surface and it has units of time. For the Dieterich-Ruina ("slowness" or "ageing") form of the law, the state evolves according to

$$\frac{\partial\theta(x,z,t)}{\partial t} = 1 - \frac{v(x,z,t)\,\theta(x,z,t)}{L(x,z)}. \tag{3}$$

In equation (2), μ_0 is the nominal friction coefficient, a and b are constants that depend on temperature (and hence depth), L is the critical slip distance for friction evolution (Figure 1) and v_0 is a normalizing constant (here $v_0 = v^\infty$).

[10] The characteristic slip distance L is a length scale over which a new population of contacts between two surfaces evolves. As mentioned earlier, laboratory values of L depend on the fault roughness and gouge width. Typical values in rock sliding experiments done to date are in the range 10^{-6}–5×10^{-4} m [*Ben-Zion*, 2003].

[11] The size of L determines a critical spatial dimension of a process or nucleation zone, h^*, and to solve the problem in the continuum limit it is necessary that $h \ll h^*$, where h is the numerical cell size [*Rice*, 1993]. This places strong constraints on the computational efficiency, since cpu time scales with the number of cells. Thus calculating slip histories within the continuum framework can be done at present only for values of L chosen to be 1–2 orders of magnitudes larger than laboratory values. Over this breakdown slip length, L, the friction coefficient μ evolves to its new steady state value

$$\mu_{ss}(x,z,t) = \mu_0 + (a(z) - b(z))\,\ln\left(\frac{v_{ss}(x,z,t)}{v_0}\right). \tag{4}$$

A stability analysis of a single degree of freedom system [*Ruina*, 1983] shows that parameters a and b define two possible stability regimes, depending on the difference $a - b$. The coefficient of friction, μ, relates the shear stress on a fault, τ, to the effective normal stress, σ_e, via

$$\tau(x,z,t) = \mu(x,z,t)\,\sigma_e(z) = \mu(x,z,t)\,(\sigma_n(z) - p(z)), \tag{5}$$

where σ_n is lithostatic normal stress on the fault and p denotes the pore pressure in the fault zone. Inserting equation (2) into (5) and differentiating the resulting equation with respect to time leads to the velocity evolution

$$\frac{\partial v(x,z,t)}{\partial t} = \left(\frac{\eta}{\sigma_e(z)} + \frac{a(z)}{v(x,z,t)}\right)^{-1} \times \left(\frac{\dot{\tau}^r(x,z,t)}{\sigma_e(z)} - \frac{b(z)\,\dot{\theta}(x,z,t)}{\theta(x,z,t)}\right), \tag{6}$$

where overdots denote time derivatives. We use the effective damping parameter $\eta = f_d \times \eta_0$, with f_d being a factor controlling quasi-dynamic ($f_d = 1$) or overdamped quasi-dynamic ($f_d \gg 1$) simulations. See *Rice* [1993] for a discussion of slip evolution with $f_d \gg 1$. In this study we apply $f_d = 10^2$ for reasons of computational efficiency. We performed simulations to investigate possible differences in response types for models with $f_d = 1$ and $f_d = 10^2$. The results are robust with respect to the conclusions drawn in this work.

[12] Temporal changes of shear stress, $\dot{\tau}^r$, are given by the sum over velocity differences, multiplied by the stiffness matrix K from equation (1), and the state evolution $\dot{\theta}$ is described by equation (3). The response of the system is thus governed by two ordinary differential equations of the state variable θ and slip rate v. Shear stress is computed using equation (1) with $\tau^0 = 100$ MPa.

2.3. Computation Technique

[13] We solve the set of three resulting first-order ordinary differential equations (equations (6) and (3) plus $\dot{u} = v$) using an explicit Runge-Kutta method with adaptive step-size control, DOP853 [*Hairer et al.*, 1993]. We use the fast Fourier transform (FFT) to compute the along-strike contribution of the stress redistribution, τ^r, executing a matrix multiplication including the stiffness kernel $K_{|i-k|,j,l}$ [*Rice*, 1993; *Stuart and Tullis*, 1995; *Rice and Ben-Zion*, 1996]. Using the FFT, the computational timescales with $(nx \log_2(nx))\, nz^2$ instead of $nx^2\, nz^2$, where nx, nz denote the number of computational cells along strike and depth, respectively, but requires nx to be a power of 2 [*Rice*, 1993].

3. Parameter Setting

[14] As pointed out by *Rice* [1993], the spatial resolution of the computational grid, h, has to be much smaller than a critical nucleation size, h^*. The condition $h \ll h^*$ is required to solve the governing equations in the continuum limit, making the computational mesh stiff enough to prevent single cells from slipping independently from neighboring computational points. The critical nucleation size for the current strike-slip geometry is found to be [*Rice*, 1993]

$$h^* = \frac{2GL}{\pi\,\sigma_e\,(b-a)_{max}}. \tag{7}$$

Previous quasi-dynamic studies employ h/h^* ratios between 0.06 [*Kato and Hirasawa*, 1999] and 0.6 [*Shibazaki and Iio*, 2003], whereas *Rice* [1993] showed that $h/h^* = 0.25$ is sufficient for conditions associated with relatively slow slip velocity. Because we employ 2-D heterogeneous distributions, we choose to min[$L(x, z)$] to determine h^* in equation (7). The maximum h/h^* ratio in this study is 0.4, a value slightly larger than that used by *Rice* [1993]. This value applies only for regions where $L = L_{min}$, but for all other regions h/h^* is smaller. Analysis of the results discussed in sections 4–6 indicates that we treat the problem in the continuum limit.

[15] The general structure of shear zones is often described by three distinct depth sections [*Scholz*, 2002; *Marone*, 1998]:

[16] 1. The topmost 3–5 km usually consist of fault gouge and damage zone, which tend to stabilize slip instabilities due to dilatancy hardening mechanisms. In simulations with RS friction this strengthening zone is usually modeled by positive $a - b$ values.

[17] 2. The depth section between $z \approx -5$ km and $z \approx -15$ km has a localized slip zone in a competent lithified rock, where most earthquakes nucleate. Exhumed fault zone structures reveal extreme localization of slip along this portion [e.g., *Chester and Chester*, 1998; *Ben-Zion and Sammis*, 2003]. Here, $a < b$ produces velocity weakening conditions allowing instabilities to nucleate.

[18] 3. Below the seismogenic depth ($z < -15$ km) the fault response is again stable due to the onset of quartz plasticity [e.g., *Scholz*, 2002]. This transition is modeled by $a - b > 0$, giving rise to a velocity-strengthening behavior.

[19] In this study we employ three different $a - b$ profiles.

[20] 1. A standard depth profile following the above common description of $a - b$ regimes at different depth sections (Figure 3a, profile 1). These conditions are chosen

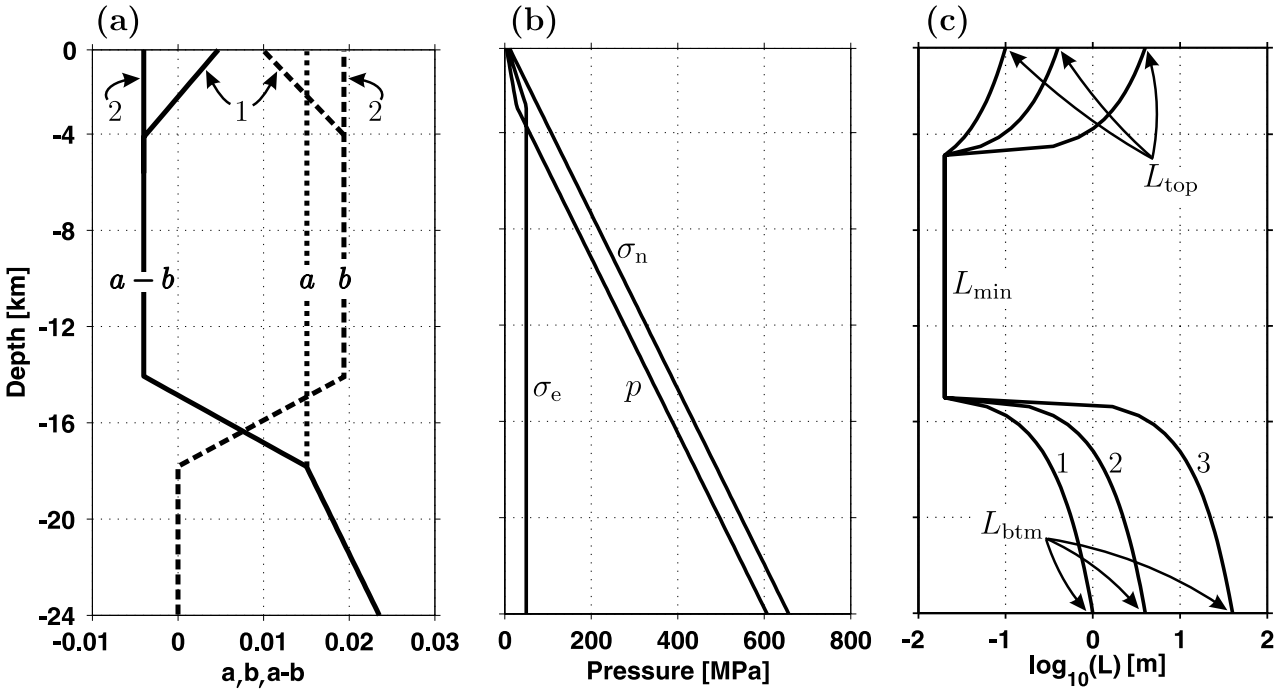

Figure 3. (a) Employed a, b, $a - b$ profiles. Profile 1, standard distribution after *Blanpied et al.* [1991]; profile 2, standard distribution without velocity-strengthening zone at shallow depth. (b) Pressure profiles. Lithostatic normal stress, σ_n, pore pressure, p, and effective normal stress, σ_e. (c) Example L profiles; 1, $\alpha = 50$; 2, $\alpha = 2 \times 10^2$; and 3, $\alpha = 2 \times 10^3$ (see equation (8)).

primarily to validate our numerical procedure against previous simulations. The depth dependency of $a - b$ has been suggested by interpreting data obtained by *Blanpied et al.* [1991]. They performed friction experiments with granite under hydrothermal conditions at various temperatures, and related their temperature-dependent data to depth using a Lachenbruch-Sass geotherm for the San Andreas fault.

[21] 2. A modified standard $a - b$ profile where we keep a constant instability-promoting $a - b < 0$ value for the entire range from the surface to $z = -15$ km (Figure 3a, profile 2). We use this approach for most of our case studies. As will be demonstrated, a distribution of the critical slip distance L with relatively large values in the shallow portion of the crust produces the same stabilizing effect that was obtained in previous works by using $a - b > 0$ above $z = -3$ km. We note that *Tse and Rice* [1986] also used $a < b$ for the shallow crust based on data from *Stesky* [1975] with a velocity weakening zone ($a < b$) down to 300°C ($z \approx -11$ km).

[22] 3. In one set of simulations where L is chosen to be a function of depth only, we treat $a - b = -0.004 = \text{const}$, so that the entire fault is in a velocity weakening regime. This allows us to isolate the effects of the applied L profile on the model response.

4. Homogeneous L Distribution Along Strike

4.1. Standard Model, Constant L

[23] To verify our numerical procedure, we compute the response of the 2-D strike-slip model to several cases with spatial distribution of RS frictional parameters similar to those used in previous studies [*Tse and Rice*, 1986; *Rice*, 1993; *Ben-Zion and Rice*, 1997; *Lapusta et al.*, 2000]. The response of such a model (MS1 in Table 1) is shown in Figure 4a; here we apply the standard depth dependent $a - b$ profile with two velocity-strengthening regions at the top and bottom of the fault and L being constant over the plane. Typical features of the slip evolution are creeping responses in the velocity-strengthening sections ($a - b > 0$) above $z = -3$ km and below $z = -14$ km, and quasiperiodic system size stick-slip events over the seismogenic depth section with velocity-weakening behavior ($a - b < 0$).

4.2. Depth-Dependent L Profiles

[24] In contrast to previous studies we interpret the average depth structure of shallow fault zones, and an associated transition from stable to unstable regimes, in terms of the critical slip distance parameter L. As can be seen from equation (2) and Figure 1, the larger L the longer two adjacent fault walls have to slide past each other for the coefficient of friction to drop to its steady state velocity-weakening value, $\mu_{ss}(v_2) < \mu_{ss}(v_1)$ for $a < b$, where v_1 and $v_2 > v_1$ denote velocity values before and after the velocity change, respectively. Therefore regions where μ does not drop below $\mu_{ss}(v_1)$ during small slip events, due to a large critical slip distance, will be effectively in a velocity-strengthening regime, although $a < b$ allows for unstable sliding.

[25] The profiles shown in Figure 3c give examples of L distributions that can stabilize the response of the fault above and below the seismogenic zone. The minimum value, L_{min}, is determined by the size of the grid to assure that in most places $h \ll h^*$. The values at the bottom and

Table 1. Overview of Models With Depth-Dependent L Profiles[a]

Model Name	L Distribution	L_{min}, m	α	$a - b$	X_{length}, km	Z_{depth}, km	nx	nz	h/h^*	Response Type	$\hat{t}$, years	Figure
MS1	const	0.02	–	profile 1	100	24	256	64	0.2	stick-slip	76.5	4
ML1	profile	0.02	50	const	100	24	512	128	0.1	stick-slip	87.6	5
ML2	profile	0.01	5×10^2	const	100	24	512	128	0.2	stick-slip	29.8	–
ML3	profile	0.02	2	const	100	24	256	64	0.2	stick-slip	145.1	–
ML4	profile	0.02	5	const	100	24	256	64	0.2	stick-slip	129.2	–
ML5	profile	0.02	10	const	100	24	256	64	0.2	stick-slip	114.6	–
ML6	profile	0.02	20	const	100	24	256	64	0.2	stick-slip	99.6	–
ML7	profile	0.02	50	const	100	24	256	64	0.2	stick-slip	93.1	4
ML8	profile	0.02	10^2	const	100	24	256	64	0.2	pattern	–	–
ML9	profile	0.02	2×10^2	const	100	24	256	64	0.2	pattern	–	6
ML10	profile	0.02	2×10^2	const	100	24	512	128	0.1	pattern	–	6
ML11	profile	0.02	5×10^2	const	100	24	256	64	0.2	pattern	–	–
ML12	profile	0.02	10^3	const	100	24	256	64	0.2	pattern	–	–
ML13	profile	0.02	2×10^3	const	100	24	256	64	0.2	pattern	–	6
ML14	profile	0.02	2×10^3	const	200	24	512	64	0.2	pattern	–	6
ML15	profile	0.02	5×10^3	const	100	24	256	64	0.2	pattern	–	–
ML16	profile	0.02	10^4	const	100	24	256	64	0.2	pattern	–	–
ML17	profile	0.02	10^5	const	100	24	256	64	0.2	pattern	–	–
ML18	profile	0.04	50	const	100	24	256	64	0.1	stick-slip	67.3	–
ML19	profile	0.04	10^2	const	100	24	256	64	0.1	creep	–	–
ML20	profile	0.04	2×10^2	const	100	24	256	64	0.1	creep	–	–

[a]Profile 1 for $a - b$ refers to Figure 3a; $\hat{t}$, interevent time; stick-slip, regular stick-slip behavior; pattern, nonuniform slip evolution; creep, the whole fault slides stably (not shown).

top of the computational region, L_{btm} and L_{top}, respectively, are determined by

$$L_{btm} = \alpha \times L_{min}$$
$$L_{top} = \max[1, 0.1 \times \alpha] \times L_{min}. \quad (8)$$

Between L_{top}, L_{min} and L_{min}, L_{btm}, the L values are interpolated linearly. To isolate the effects of such an employed L profile, we keep $a - b = -0.004$ = const, although $a > b$ below $z \sim -15$ km might be more realistic. Figure 4b illustrates the slip evolution in response

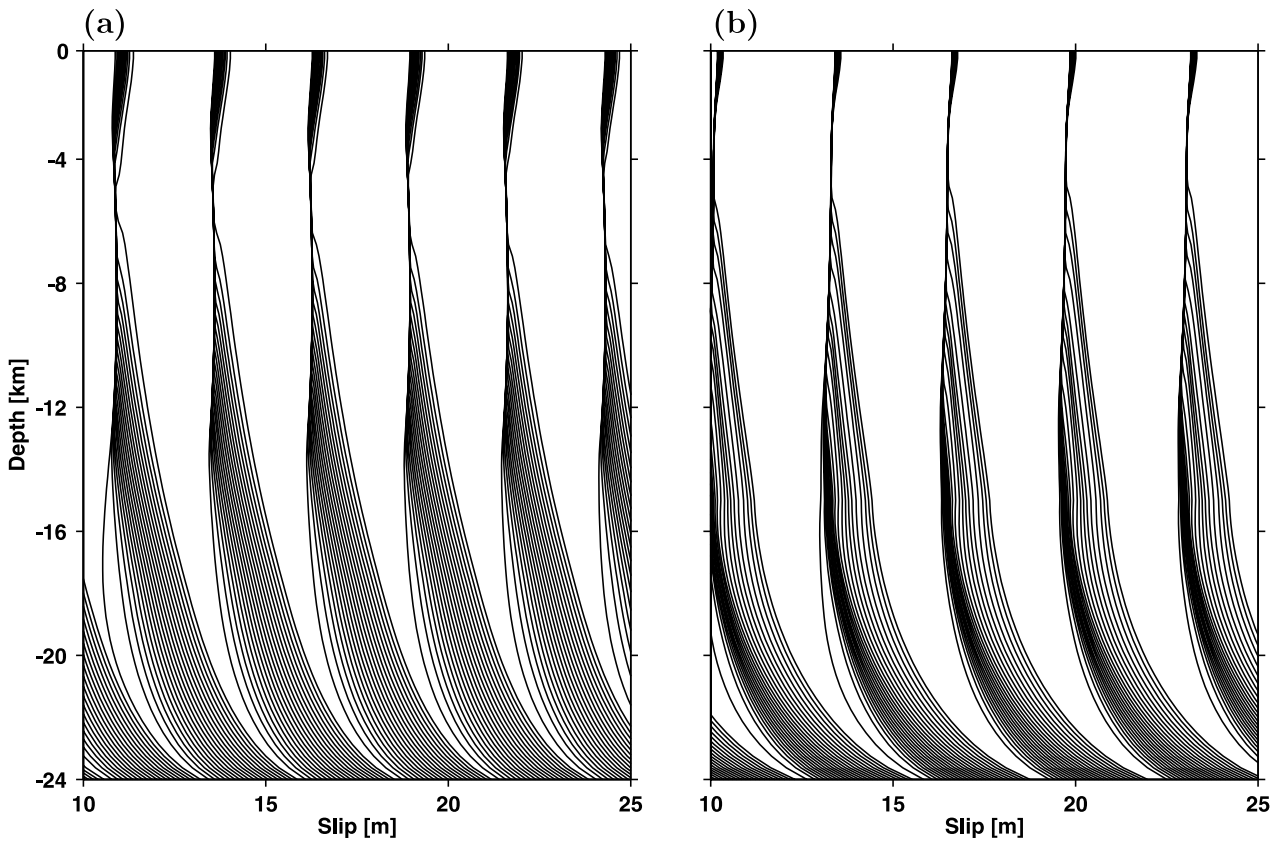

Figure 4. (a) Stick-slip response of model MS1 in Table 1. Applied $a - b$ profile 1 from Figure 3a, L = 0.02 m = const, h/h^* = 0.2, $\eta = 10^2 \times \eta_0$. (b) The same characteristic behavior obtained for model ML7, where $a - b = -0.004$ = const, L_{min} = 0.02 m, α = 50 (profile 1 of Figure 3c), h/h^* = 0.2, $\eta = 10^2 \times \eta_0$. Lines are drawn every 4 years.

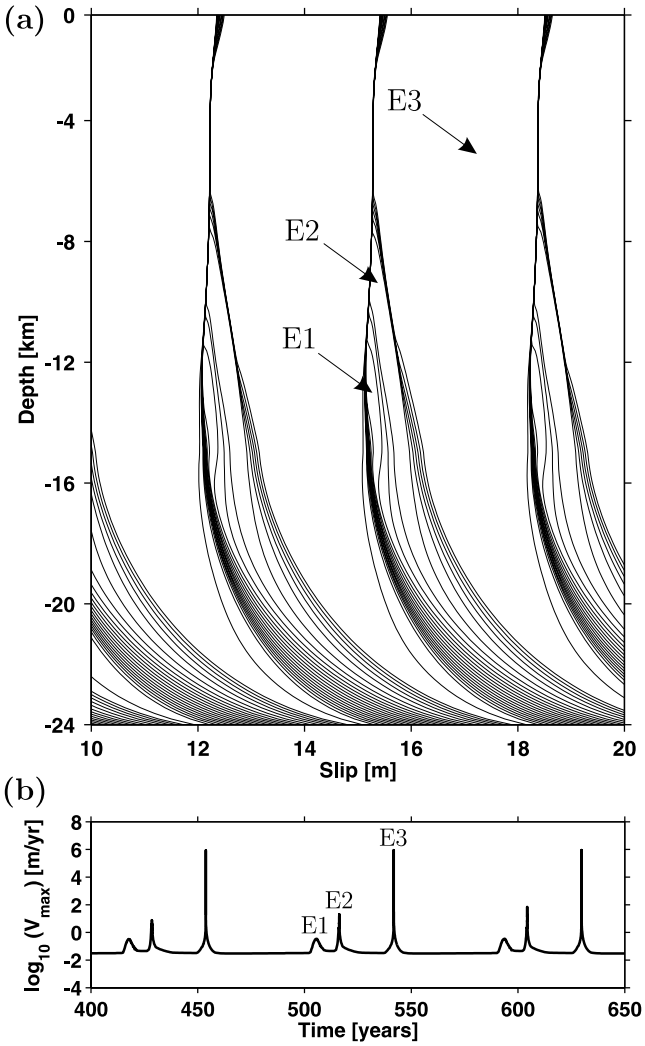

Figure 5. (a) Slip evolution of model ML1 in response to $a - b = -0.004$ = const, $L_{\min} = 0.02$ m, $\alpha = 50$ (profile 1 of Figure 3c), $h/h^* = 0.2$, $\eta = 10^2 \times \eta_0$. E1, E2 mark successive smaller instabilities around $z = -12$ km prior to the main slip event, E3. Lines are drawn every 2 years. (b) Corresponding maximum velocity evolution. Two smaller events are clearly identifiable 26 and 37 years prior to the characteristic slip event, respectively.

to the employed L profile 1 in Figure 3c with $\alpha = 50$, i.e., $L_{\min} = 0.02$ m, $L_{\text{btm}} = 1$ m and $L_{\text{top}} = 0.1$ m, respectively (ML7 in Table 1). Although the creeping behavior at the surface is less pronounced and coseismic slip extends further down compared to the standard model, these simulations match qualitatively the regular stick-slip behavior generated with the standard parameter setup of Figure 4a.

[26] To investigate additional properties of the response pattern, we perform several simulations with different $L_{\min}$ and α, as well as different spatial dimension (X_{length}) and discretization (h) of the model. To examine the effect of decreasing h/h^*, we repeat the simulation leading to Figure 4b, employing the same parameters except doubling the number of cells along strike and depth, thus reducing h/h^* from 0.2 to 0.1. As can be seen in Figure 5 (ML1 in Table 1), the response to the applied reduction in h/h^* duplicates the overall slip evolution of Figure 4b. In addition, the more refined calculations produce two smaller events (E1, E2 in Figure 5) nucleating 26 and 37 years prior to the 'main shock', respectively. Note that the tendency for this behavior can also be seen in the response to the original model where $h/h^* = 0.2$ (Figure 4b), i.e., the slip profiles show a slightly different temporal evolution compared to the standard model (Figure 4a). The discrepancy between the two models with $h/h^* = 0.2$ and 0.1, respectively, raises the question whether the obtained numerical solution converged to the "true" one. *Lapusta et al.* [2000] found that in fully elastodynamic approach h/h^* has to be smaller than 0.025 to converge to the underlying model response. Our quasi-dynamic simulations can be done with a coarser grid, although our employed cell size is apparently not sufficiently small to obtain results that are fully independent of the discretization. Some of the small-scale features of our results may therefore depend on the employed grid. However, the overall first-order results (e.g., slip versus depth profiles with creeping and stick-slip regions) are stable with regard to finer discretizations.

[27] The average repeat time, $\hat{t}$, of the characteristic slip events in the seismogenic portion of the fault is a decreasing function of α. For $L_{\min} = 0.02$ m, $h = 100/256$ km, $h/h^* = 0.2$ and $\alpha = 2,5,10,20$ and 50 we obtain $\hat{t} = 145.1, 129.2, 114.6, 99.6$ and 93.1 years, respectively (ML3-ML7 in Table 1). The decrease in $\hat{t}$ reflects the growing disorder as the system approaches a change in the response type. The change from system-size events to more irregular response type associated with $\alpha = 50$ (ML7) and $\alpha = 100$ (ML8), respectively, marks the transition in behavior for models with $L_{\min} = 0.02$ m. The result shown in Figure 5 for $\alpha = 50$ and $h = 100/512$ km $\rightarrow h/h^* = 0.1$, has $\hat{t} = 87$ years, a slightly smaller value than 93.1 years of the $h/h^* = 0.2$ simulation. The origin for the difference of 4 years is the additional stress drops of the two small events associated with each main event, leading to shorter interevent times of the main events.

[28] With the given spatial discretization of the model ($h = 391$ m) we perform additional numerical experiments for increasing values of α, ranging from 10^2–10^5 (ML8-9, ML11-13, ML15-17 in Table 1). In contrast to the regular stick-slip response to the applied L profiles of Figures 4b and 5, slip evolution for $\alpha > 50$ tend to be more irregular. Figure 6 gives a comparison of event sequences at $z = -10$ km for several parameter sets.

[29] Figures 6a and 6b show responses to identical parameter sets $L_{\min} = 0.02$ m, $\alpha = 2 \times 10^3$, $h/h^* = 0.2$ on 100 km and 200 km long strike-slip fault zones, respectively (ML13, ML14 in Table 1). The small-scale features of the generated slip pattern do not coincide, but both panels show similar characteristic behavior including irregular slip events of different size. In particular, the seismic slip of 'large' events is of the same order of magnitude, indicating that this quantity is independent of the fault dimension. Figure 6c (ML9 in Table 1) presents slip evolution to a set of parameters which differs only in $\alpha = 2 \times 10^2$ from those producing the results shown in 6a. We find that even for $\alpha =$

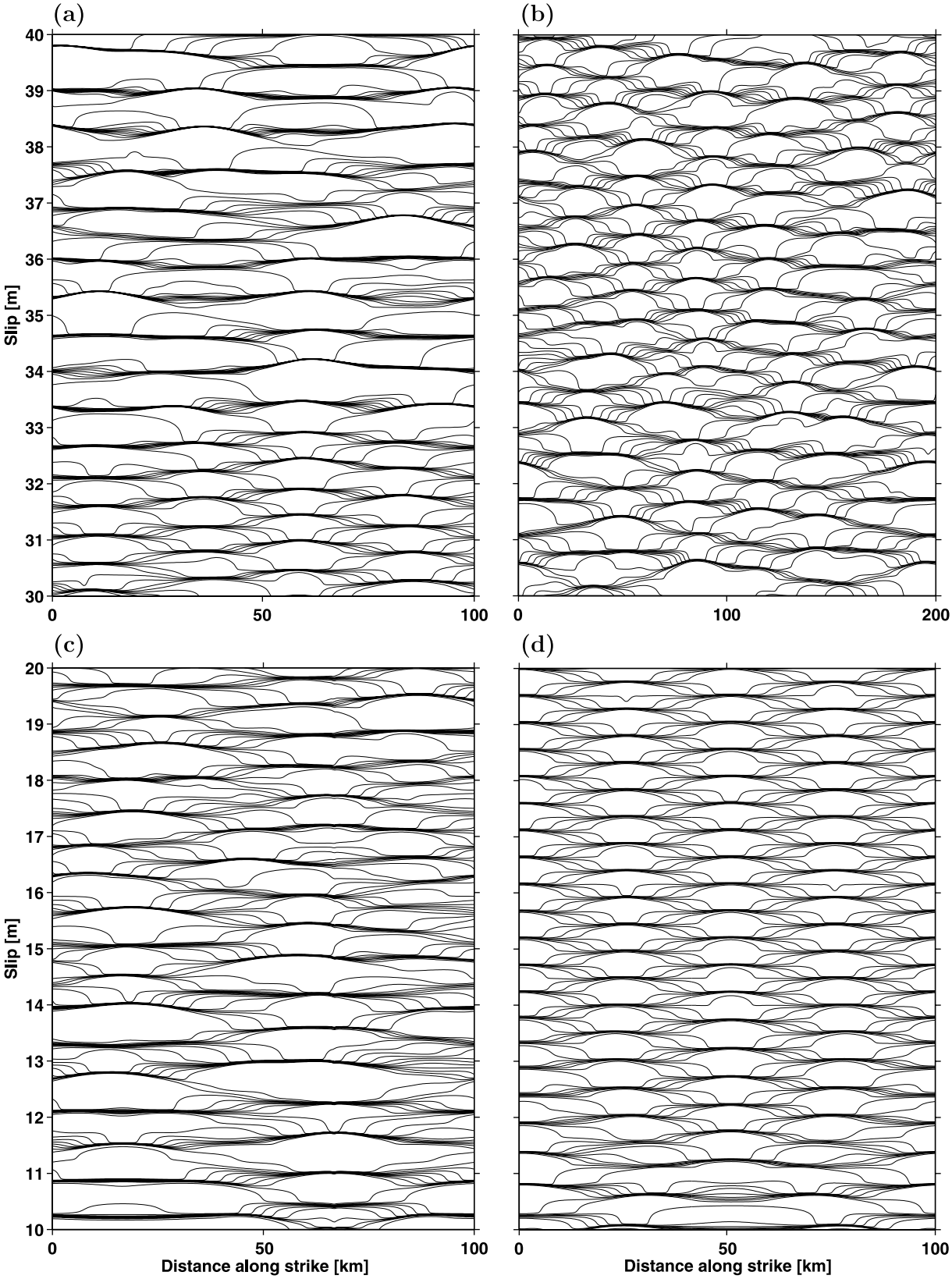

Figure 6. Slip evolutions of models with $L_{\min}$ = 0.02 m, $a - b = -0.004$ = const, $\eta = 10^2 \times \eta_0$. (a) Model ML13, $\alpha = 2 \times 10^3$ (profile 3 in Figure 3c), h = 100/256 km, h/h^* = 0.2. (b) Model ML14, $\alpha = 2 \times 10^3$ (profile 2 in Figure 3c), h = 200/512 km, h/h^* = 0.2. (c) Model ML9, $\alpha = 2 \times 10^2$ (profile 2 in Figure 3c), h = 100/256 km, h/h^* = 0.2. (d) Model ML10, $\alpha = 2 \times 10^2$ (profile 2 in Figure 3c), h = 100/512 km, h/h^* = 0.1. Slip horizons are extracted at constant seismogenic depth ($z = -10$ km). Lines are drawn every 2 years.

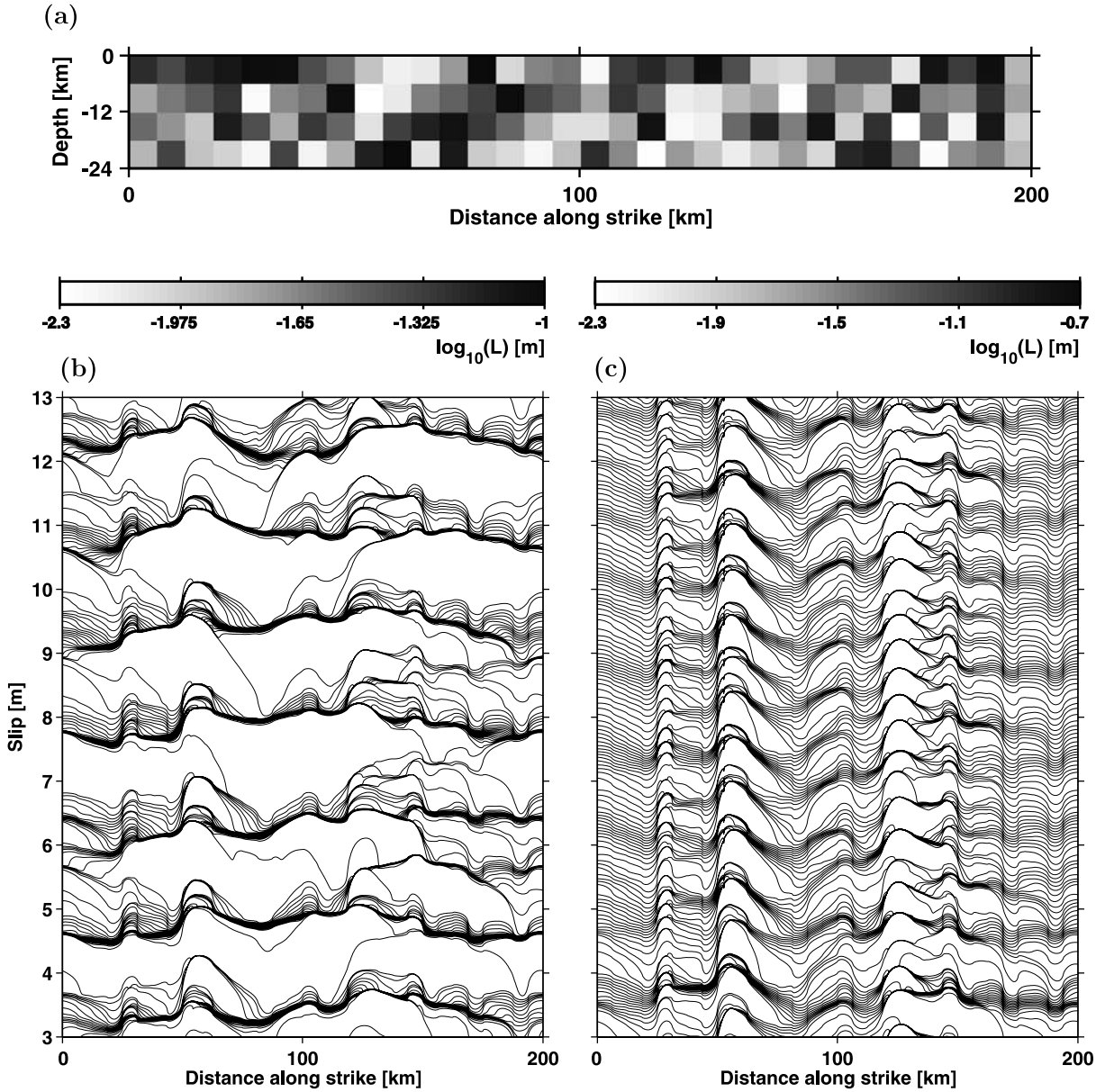

Figure 7. (a) Typical realization of a heterogeneous L distribution. (b) Response of model MP1 to the L values shown in (a) with $L \in \log_{10}([0.005, 0.1])$ m. (c) Model response of MP2 with different L_{max}, $L \in \log_{10}([0.005, 0.2])$ m. Slip profiles are shown at $z = -9$ km. Parameters for Figures 7b and 7c are $h/h^* = 0.4$, $\eta = 10^2 \times \eta_0$, $a - b$ profile 2 from Figure 3. Lines are drawn every 2 years. Note the creeping sections for larger L_{max} in Figure 7c.

10^5 the pattern does not change significantly, suggesting that irregular slip patterns are a result of a constant $a - b$ environment where instabilities are allowed to occur, and L depth distributions reflecting fault zone structure. Figure 6d displays the response of a system having the same parameter set that leads to solution 6c except nx and nz have been doubled, thus reducing h/h^* from 0.2 to 0.1 (ML10 in Table 1). After the first few cycles the response develops a quasiperiodic pattern, where two events of equal size at x = 25 km and 75 km alternate with a doublet at x = 0 km and 50 km, respectively.

[30] The resulting difference of models ML9 (Figure 6c) and ML10 (Figure 6d) illustrates again that we do not converge with the employed grid to a unique underlying solution on all scales of the response. However, the persistence of the irregular slip patterns over 3 orders of magnitudes in α, and similar amount of slip in the main seismic events, indicate that these features represent genuine aspects of the model response related to the employed L distribution with depth. In addition to the results shown in Figure 6, we investigated slip evolution of a system with L_{min} = 0.04 m (ML18-20 in Table 1). For h = 100/256 km, $a - b = -0.004$ = const and $\alpha \leq 50$ the simulations produce a stick-slip behavior over the seismogenic depth section, whereas for $\alpha > 50$ the entire fault slips stably. Table 1 summarizes the sets of param-

Table 2. Overview of Models With 2-D Chessboard L Distributions[a]

Model	L Pattern	L_{min}, m	L_{max}, m	$a - b$	Number of Patches	X_{length}, km	Z_{depth}, km	nx	nz	h/h^*	Response Type	r	χ	Figure
MP1	chessboard	0.005	0.1	profile 2	32 × 4	200	24	1024	256	0.4	pattern	–	–	7
MP2	chessboard	0.005	0.2	profile 2	32 × 4	200	24	1024	256	0.4	pattern	–	–	7
MP3	chessboard	0.005	0.1	profile 2	8 × 1	200	24	1024	256	0.4	pattern	0.31	0.44	–
MP4	chessboard	0.005	0.1	profile 2	8 × 1	200	24	1024	256	0.4	pattern	0.33	0.42	9, 10, 11
MP5	chessboard	0.005	0.1	profile 2	16 × 2	200	24	1024	256	0.4	pattern	0.47	0.22	9, 10, 11, 13
MP6	chessboard	0.005	0.1	profile 2	16 × 2	200	24	1024	256	0.4	pattern	0.49	0.30	13
MP7	chessboard	0.005	0.1	profile 2	32 × 4	200	24	1024	256	0.4	pattern	1.01	0.25	13
MP8	chessboard	0.005	0.1	profile 2	32 × 4	200	24	1024	256	0.4	pattern	0.69	0.33	9, 12, 13
MP9	chessboard	0.005	0.2	profile 2	32 × 4	200	24	1024	256	0.4	pattern	1.07	0.05	12
MP10	chessboard	0.005	0.1	profile 2	64 × 8	200	24	1024	256	0.4	pattern	0.90	0.35	–
MP11	chessboard	0.005	0.1	profile 2	64 × 8	200	24	1024	256	0.4	pattern	0.96	0.28	9, 10, 11

[a]Profile 2 for $a - b$ refers to Figure 3a.

eters employed in different numerical simulations and the corresponding system response.

5. Heterogeneous L Distribution Along Strike

5.1. Typical Implementation Example

[31] In this section we explore slip evolutions of systems with heterogeneous L distributions along strike and depth. Field observations of fault traces in strike-slip environments and laboratory measurements of fracture surfaces show geometrical irregularity over many scale lengths. A variety of multidisciplinary observations [*Ben-Zion and Sammis*, 2003, and references therein] suggest that the range of size scales of geometrical irregularities decreases with the cumulative slip on a fault. Previous numerical simulations indicate [*Ben-Zion and Rice*, 1995; *Ben-Zion*, 1996; *Zöller et al.*, 2005c] that the range of size scales characterizing the fault heterogeneities can act as an effective tuning parameter of the fault dynamics. On the basis of the above observational and theoretical results, 2-D L distributions with different ranges of size scales may be used to represent faults at different evolutionary stages [e.g., *Wesnousky*, 1994]. Geometrical heterogeneity along the fault trace may also influence the normal stress distribution, which in turn could give rise to complex dynamics [*Ben-Zion*, 2001; *Perfettini et al.*, 2003]. However, here we examine effects associated with heterogeneous distributions of L and adopt the traditional assumption that the normal stress does not change with slip. In the following sections we focus primarily on general features associated with 2-D heterogeneous L distributions. A systematic study of model realizations representing faults at different evolutionary stages is left for a future work.

[32] To obtain a basic understanding of the model response, we begin with some cases that have chessboard patterns of L values. A typical implementation example is given in Figure 7a, where the 200 × 24 km^2 fault plane is divided into 32 × 4 patches along strike and dip, respectively, each consisting of 32 × 32 cells. The minimum applied value for the critical slip distance L_{min} is governed by the spatial discretization of the computational grid. To investigate the effect of different L_{max} values, we divide the interval $\log_{10}([L_{min}, L_{max}])$ equally into 32 × 4 = 128 values and randomly assign one L value to each cell of a certain patch. We employ L_{min} = 0.005 m, leading to h/h^* = 0.4 in patches having L_{min} and smaller values in all other patches. Since the 2-D L function in Figure 7a has no particular depth dependence, we apply an $a - b$ profile that stabilizes fault slip at depth (Figure 3a, profile 2). Figures 7b and 7c show slip profiles along strike at $z = -9$ km with $L \in \log_{10}([0.005, 0.1])$ m and $L \in \log_{10}([0.005, 0.2])$ m, respectively (MP1, MP2 in Table 2), applied to the pattern shown in Figure 7a. The slip evolution in Figure 7c with a slightly broader range of size scales shows somewhat a larger diversity of response. However, the larger length scales that are present in the distribution leading to Figure 7c produce a stabilizing effect that lead to more creeping regions. In between these creeping regions smaller slip events can be identified creating nonstationary spatiotemporal slip pattern (e.g., at x = 120–180 km). Because of the stabilizing effect of L_{max} = 0.2 m, we employ in all subsequent models $L \in \log_{10}([0.005, 0.1])$ m to study the response to different degrees of L heterogeneities.

5.2. Extracting a Catalog

[33] To describe seismicity on a fault with different L distributions, we have to determine quantities that are listed in typical earthquake catalogs. We extract a seismic catalog from the continuously simulated slip velocities generated by our numerical experiments using the following criteria for a seismic event:

[34] 1. A numerical cell is considered to slip seismically when its velocity is equal to or greater than a threshold velocity, v^{trs}, defined to be 10^3 or 10^4 times the load velocity v^{∞}.

[35] 2. A compact zone of minimum 10–20 cells with $v \geq v^{trs}$ is required to determine the smallest event size, since we treat the system in the continuum limit. Note that the diameter of the resulting patch (600–854 m) is smaller than the dimension of the nucleation zone h^* in places where L is large ($h^* \approx 9.5$ km for $L = L_{max} = 0.1$ m), but comparable to h^* where the critical slip distance is small ($h^* \approx 480$ m for $L = L_{min} = 0.005$ m).

[36] 3. A seismic event ends if $v < v^{trs}$ for all cells involved.

[37] 4. The hypocenter is the cell location whose sliding velocity satisfies first $v \geq v^{trs}$ at the onset of slip instability.

[38] 5. The event size is measured by the scalar potency P (sum of seismic slip times rupture area in [km^{2}cm]) associated with the seismic slip [*Ben-Zion*, 2003]. The corresponding event magnitude is obtained by the empirical

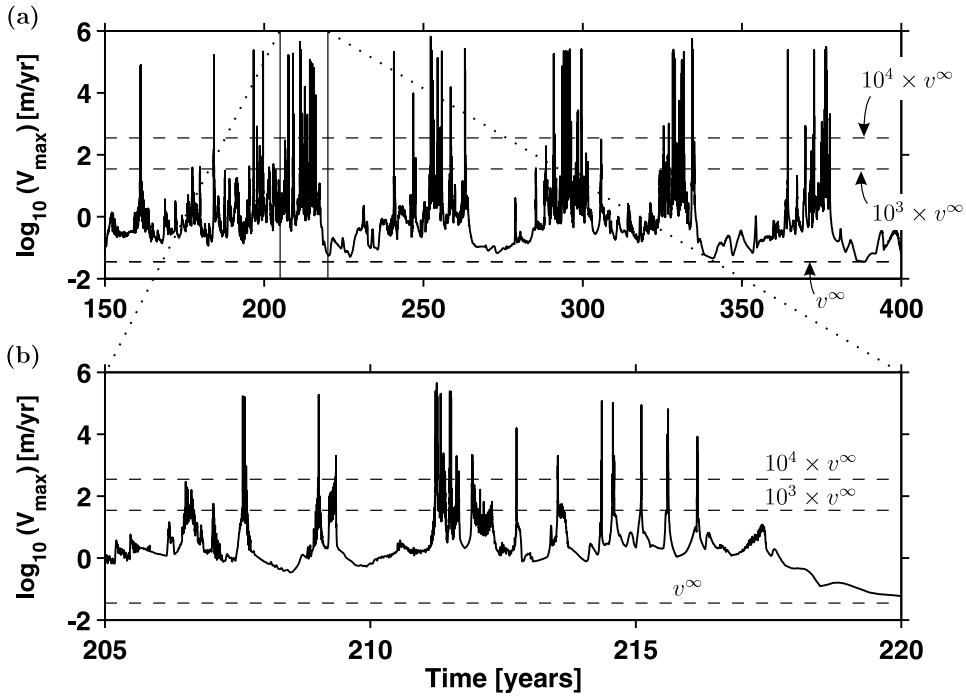

Figure 8. (a) Example evolution of maximum velocity as a function of simulated time for a typical experiment, indicating load velocity v^{∞} and two possible threshold velocities. (b) Blowup of seismically active period between t = 205 and t = 220 years.

scaling relation of *Ben-Zion and Zhu* [2002] for events larger than $M_L = 3.5$

$$\log_{10}(P) = 1.34\,M_L - 5.22, \tag{9}$$

where M_L is the local magnitude of California.

[39] Figure 8 shows maximum slip velocity as a function of time on a model fault for a simulated interval of 250 years. The three dashed lines indicate v^{∞} and threshold velocities $10^3 \times v^{\infty}$ and $10^4 \times v^{\infty}$, respectively. We tested several realizations of slip zone sizes consisting of 10 and 20 cells as well as other velocity thresholds and concluded that the obtained statistics of model earthquakes are not very sensitive to the precise choices of these parameters. Thus we will use a minimum zone of 10 connected cells and $v^{\mathrm{trs}} = 10^3 \times v^{\infty}$ to extract seismic events from our simulation data.

[40] In order to monitor the stress evolution on the fault, we follow *Ben-Zion et al.* [2003a] by using several stress functions related to seismicity and criticality. The average stress on a fault, AS, tracks the evolution associated with the remote loading:

$$\mathrm{AS}(t) = \frac{1}{N}\sum_{i=1}^{N}\tau_i(t), \tag{10}$$

where $\tau_i(t)$ denotes stress at cell i and time t and N is the number of cells in the upper 15 km of the fault. The standard deviation of stress, SD, is used to estimate the range of stress fluctuations on the fault,

$$SD(t) = \sqrt{\frac{1}{N}\sum_{i=1}^{N}\left(\tau_i(t) - \mathrm{AS}(t)\right)^2}. \tag{11}$$

We calculate AS and SD for $z > -15$ km to exclude minor stress variations in the stable sliding part of the model fault. To test the hypothesis of accelerated seismic release prior to large or system wide events, we monitor the cumulative Benioff strain

$$\varepsilon(t) = \sum_{i=1}^{N(t)}\sqrt{E_i(t)}, \tag{12}$$

where E_i is the energy of the ith event and $N(t)$ is the number of events at time t. We compute the change in strain energy according to *Kostrov* [1974]

$$E = \frac{1}{2}\Delta\tau\bar{u}A, \tag{13}$$

where $\Delta\tau$, $\bar{u}$ and A denote stress drop, mean slip and rupture area, respectively. In addition, we calculate seismic coupling, χ, to measure the partition of strain release between seismic and aseismic components,

$$\chi = \frac{\text{seismic slip}}{\text{total slip}}. \tag{14}$$

5.3. Model Results

[41] To compare slip evolutions for various degrees of fault heterogeneity, we use four classes of 2-D L distributions (Figure 9) approximating different ranges of size scales. Patterns P1–P4 consists of 8 × 1, 16 × 2, 32 × 4 and 64 × 8 patches along strike and depth, respectively. They are distributed on a numerical fault plane discretized

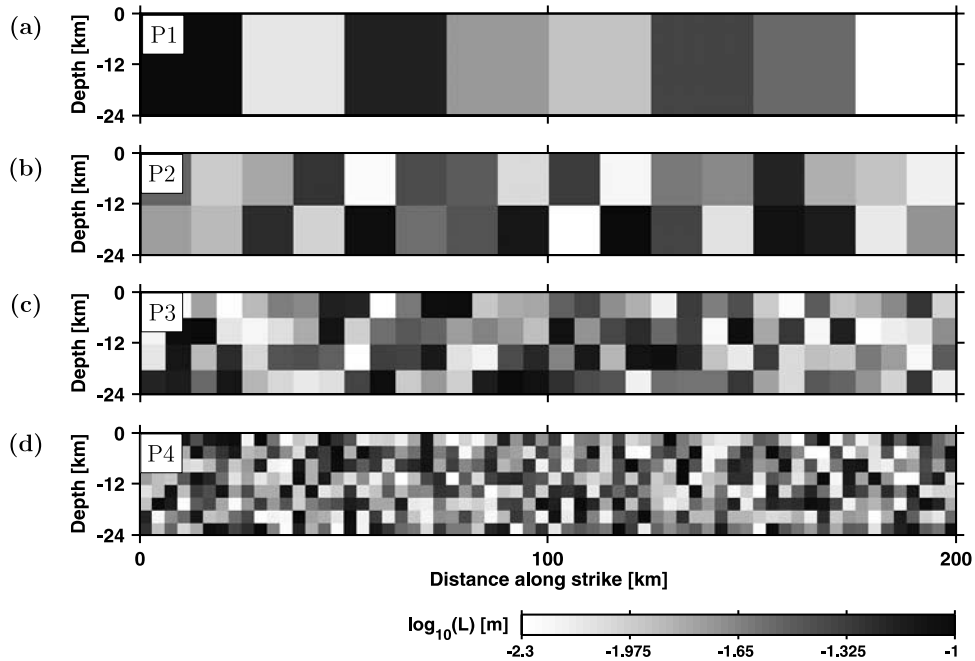

Figure 9. Examples of heterogeneous L distributions on a typical 200 km × 24 km fault zone with nx = 1024, nz = 128, showing four model patterns P1–P4 with different degrees of heterogeneity. (a) Model MP4, 8 × 1 patches; (b) model MP5, 16 × 2 patches; (c) model MP8/MP9, 32 × 4 patches; and (d) model MP11, 64 × 8 patches. If not specified otherwise, $L \in \log_{10}([0.005, 0.1])$ m.

into 1024 × 128 cells covering 200 km × 24 km. We use the $a - b$ profile without a stable-unstable transition at $z = -3$ km (Figure 3a, profile 2) to focus on effects due to the variability in L across the fault. Values for L are bounded by $L_{\min}$ = 0.005 m and $L_{\max}$ = 0.1 m. Figure 10 compares basic properties of seismicity generated by models MP4, MP5 and MP11 (Figures 9a, 9c, and 9d). The histograms on the left panel display the number of hypocenters as a function of L at the hypocenter location. Clearly, earthquakes tend to nucleate in regions where L is small. Most events nucleate where L is in the lower 25% of the interval $\log_{10}([L_{\min}, L_{\max}])$, because the nucleation size $h^* = f(L)$ is small and fluctuations can grow unstable more easily.

[42] The frequency size (FS) statistics demonstrate the capability of the chosen approach to generate event sizes over a broad range of magnitudes. For a reference we plot the slope of FS statistics characterizing global strike-slip events shallower than 50 km [*Frohlich and Davis*, 1993]. The employed spatial discretization allows for a minimum magnitude of M_L = 3.8. This effect is responsible for the curvature of data points at small magnitudes generated by models MP5, MP11, whereas finite size effects of the fault's seismogenic width are evident in the curvature at large magnitudes. However, the more patches and L values are employed, the more the simulated slope approaches the reference observed one.

[43] Figure 10 (right) displays fundamental differences in seismicity evolution. The responses to different realizations of L distributions reveal that larger heterogeneity leads to a higher productivity of seismic events. With N and t_s being the number of generated events and simulated time neglecting initial quiescence, respectively, the seismicity rate

$$r = \frac{N}{t_s} \tag{15}$$

increases from the most homogeneous case (MP4, Figure 10a) to the case of strongly heterogeneous (MP11, Figure 10c) L distribution (see Table 2). The seismic coupling χ also scales with the number of imposed L values, leading to 0.44/0.42, 0.30/0.22 and 0.35/0.28 for two realizations for each of P1, P2, P4 (see Figure 9) model, respectively. This indicates the tendency of faults with large-scale irregularities to relieve slip deficits more seismically than faults with small-scale irregularities (MP3–MP6, MP10–11 in Table 2).

[44] Common to all the seismicity evolutions is the quasi-cyclic behavior where periods of quiescence alternate with periods of clustered seismic activity. We observe that within active periods regular patterns cannot be identified. Furthermore, no aftershock sequences occur in the generated seismicity evolutions. Thus the present parameterization and discretization of the model space is not sufficient to produce all features of natural seismicity. However, future simulations allowing for smaller events might be capable to do so. Figure 11 shows the evolution of stress functions AS and SD in response to MP4 (Figure 11a), MP5 (Figure 11b), and MP11 (Figure 11c). The average stress on faults with large-scale heterogeneities (MP4) evolves in an irregular pattern of pronounced stress drops, accompanied by corresponding strong signals in SD (Figure 11a). With increasing degree of heterogeneity (MP5, MP11) the shape of function AS approaches a more regular saw-tooth-like

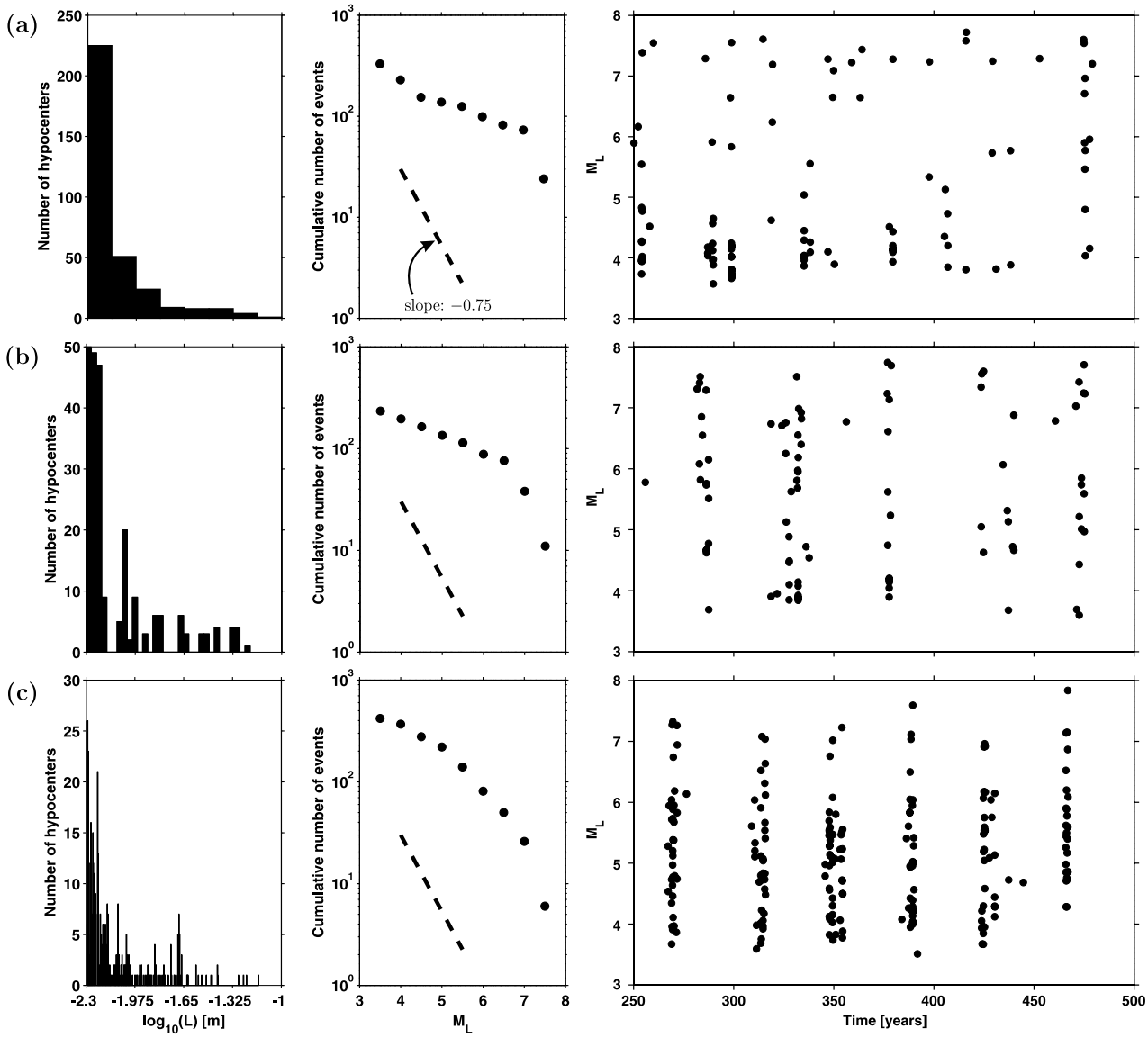

Figure 10. Statistics in response to L distributions of models (a) MP4 (8 × 1), (b) MP5 (32 × 4), and (c) MP11 (64 × 8) shown in Figures 9a, 9b, and 9d. (left) Distribution of hypocenters as a function of L at the hypocenter. (middle) FS statistics. (right) Seismicity evolution. Decrease of bar width in histograms reflects finer discretization of the interval $\log_{10}([L_{\min}, L_{\max}])$ with increasing number of patches.

behavior (Figures 11b and 11c). The accompanying evolution of SD is interrupted by sharp fluctuations that are less pronounced for larger heterogeneity (Figure 11c). Simultaneously, small-scale fluctuations of SD increase significantly. Thus the evolution of AS and SD provide a complementary view of the seismicity evolution shown in Figure 10. In particular, the occurrence of large earthquakes dominate large-scale fluctuations in AS, whereas the rate of small events controls the small-scale features in SD. The stress functions *AS* and SD in response to MP4, MP5 and MP11 are comparable to the output of model F with realistic dynamic weakening in *Ben-Zion et al.* [2003a]. In contrast, the evolution of AS and SD in model FC of *Ben-Zion et al.* [2003a] with zero critical dynamic weakening exhibit highly irregular small-amplitude fluctuations. The present implementation of heterogeneities in the continuum limit is not sufficient to produce such highly fluctuating stress functions. However, future implementations with broader ranges of size scales may produce such results [*Ben-Zion*, 1996; *Zöller et al.*, 2005c].

[45] In Figure 12 we compare results obtained by two different simulations, using the same 32 × 4 L pattern (Figure 9c) but $L_{\max}$ = 0.1 m and $L_{\max}$ = 0.2 m, respectively (MP8, MP9 in Table 2). The number of hypocenters as a function of L at the hypocenter location as well as the obtained FS statistics (Figure 12a) show no significant difference. However, the stress functions AS and SD differ significantly for these two realizations. First, the average stress of the model with $L_{\max}$ = 0.1 m develops more distinct stress drops comparable to those of models MP5 and MP11 (Figures 11b and 11c). The same L pattern with $L_{\max}$ = 0.2 results in a higher temporal average of AS with

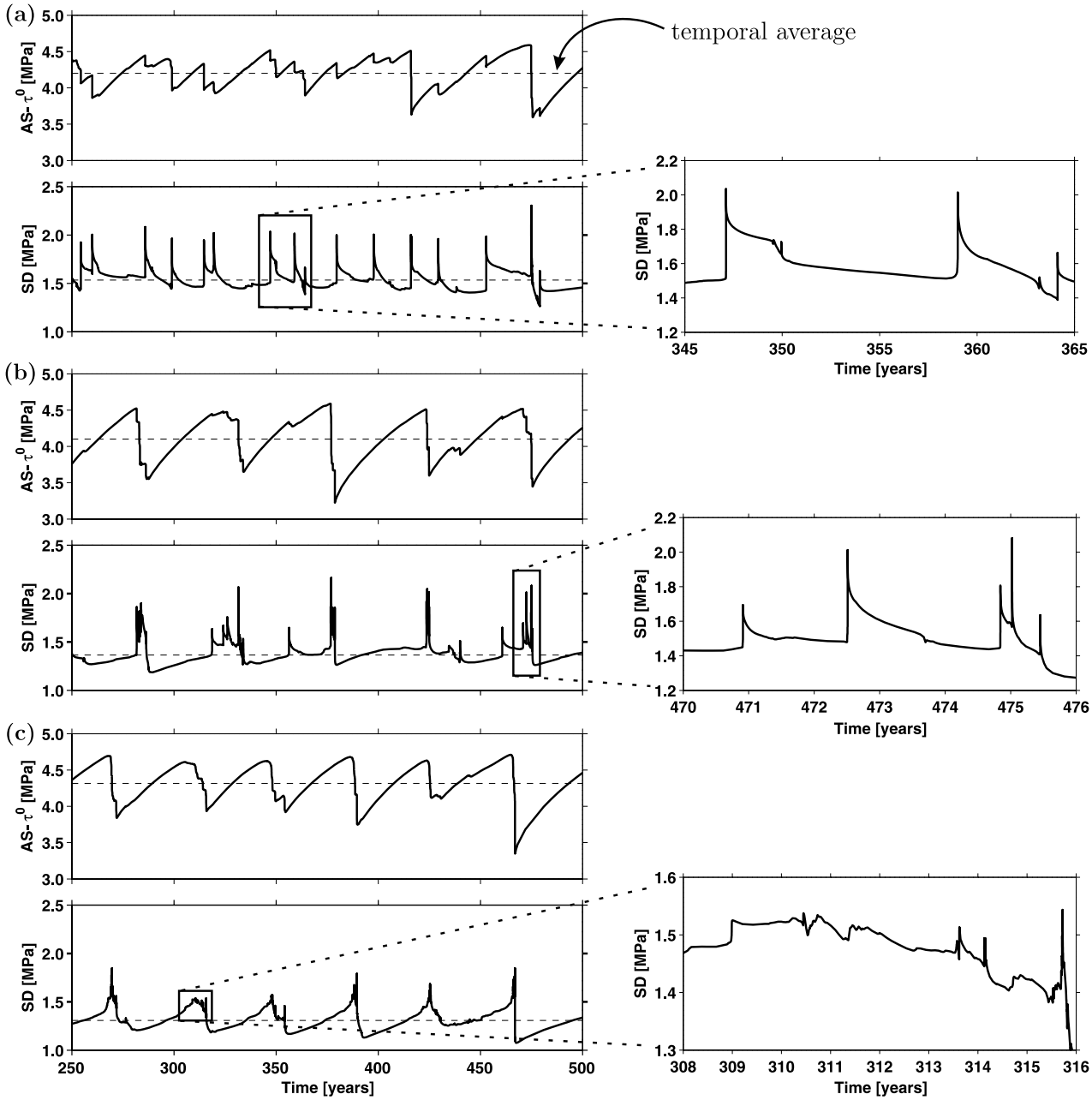

Figure 11. Average stress (AS) and its standard deviation (SD) in the top 15 km of the fault. (a), (b) and (c) Response to models MP4, MP5, MP11 shown in Figures 9a, 9b, and 9d, respectively.

less pronounced variabilities, developing a sinusoidal behavior. Second, the SD for L_{max} = 0.1 m shows less fluctuations in interseismic periods but more distinct signals when large events occur (Figure 12c). For L_{max} = 0.2 m, the SD shows small-scale fluctuations at all times but less clear deviations at large events. The temporal dependence of AS and SD can be explained by the temporal distribution of seismicity (Figure 12d). For L_{max} = 0.1 m the quasiperiodic evolution of seismicity matches the previously discussed results with L_{max} = 0.1 m (Figure 10). For L_{max} = 0.2 m, the periods of seismic quiescence are less pronounced, but seismicity still occurs clustered in time.

[46] The critical point theory implies that large earthquakes are preceded by an increase in stress correlation in the volume hosting the catastrophic event [e.g., *Sornette and Sammis*, 1995; *Zöller and Hainzl*, 2002]. Larger stress correlations are caused by an increased occurrence of intermediate and moderate size earthquakes [*Jaumé and Sykes*, 1999; *Ben-Zion and Lyakhovsky*, 2002]. According to the critical point theory the cumulative Benioff strain, ε, deduced from our synthetic catalogs should follow a power law increase prior to a large event [*Bowman et al.*, 1998; *Sornette*, 2002; *Mora and Place*, 2002]. An example of ε from a seismically active period is shown in Figure 12e. We observe an increase of ε prior to a large event for both models at t = 376.3 years and t = 351.3 years, respectively. The quality of the data is at least comparable to the Loma Prieta example of *Bowman et al.* [1998]. Other pre main

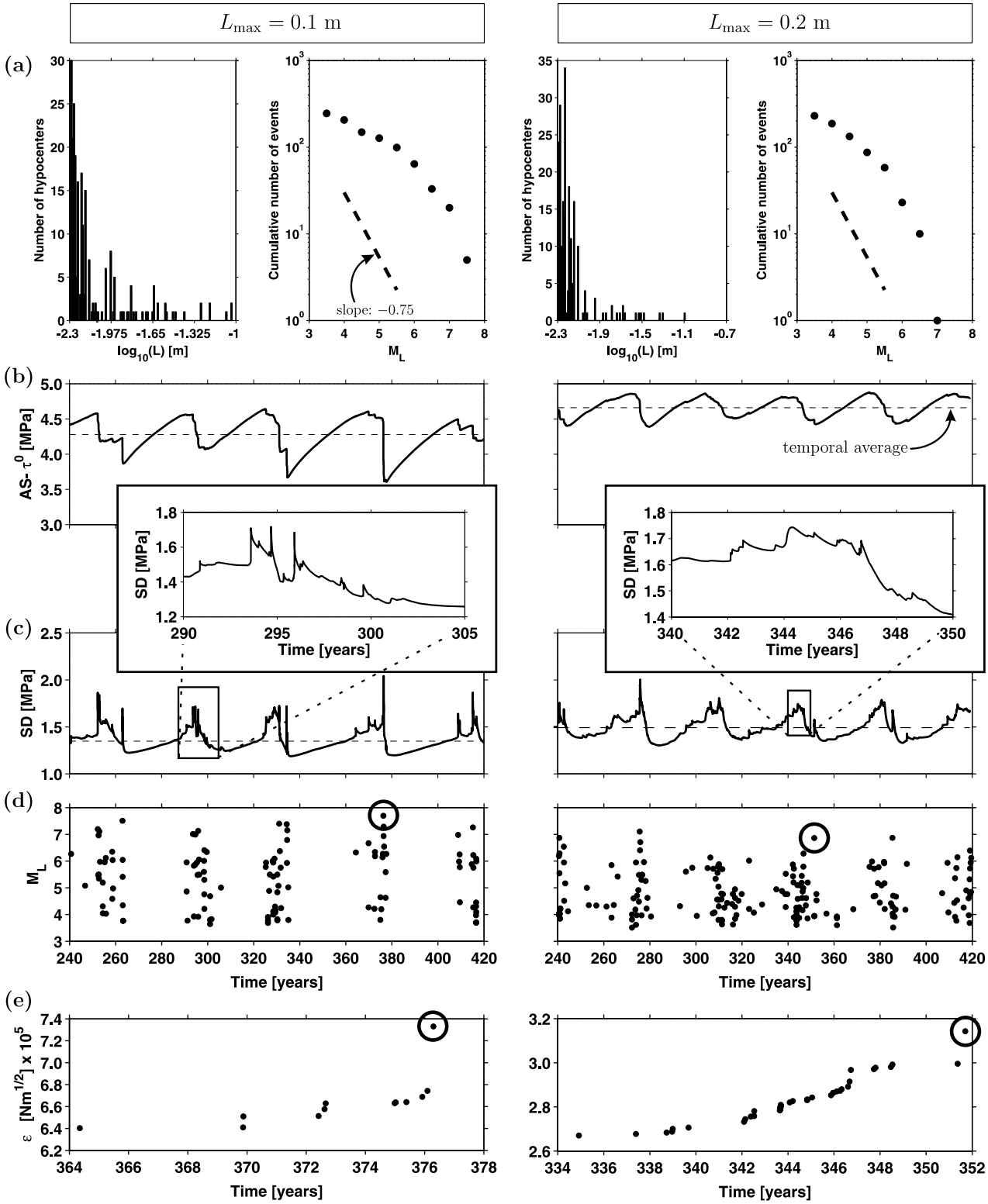

Figure 12. Results of two simulations with identical L pattern (32 × 4 patches, Figure 9c). (left) Model MP8, $L \in \log_{10}([0.005, 0.1])$ m; (right) model MP9, $L \in \log_{10}([0.005, 0.2])$ m. (a) Number of hypocenters as a function of $\log_{10}(L)$ at the hypocenter and FS statistics. Temporal evolution of (b) average stress (AS) and (c) standard deviation of stress (SD) in the top 15 km of the fault. (d) Seismicity evolution. (e) Cumulative Benioff strain release. Circles in Figures 12d and 12e mark corresponding large earthquakes.

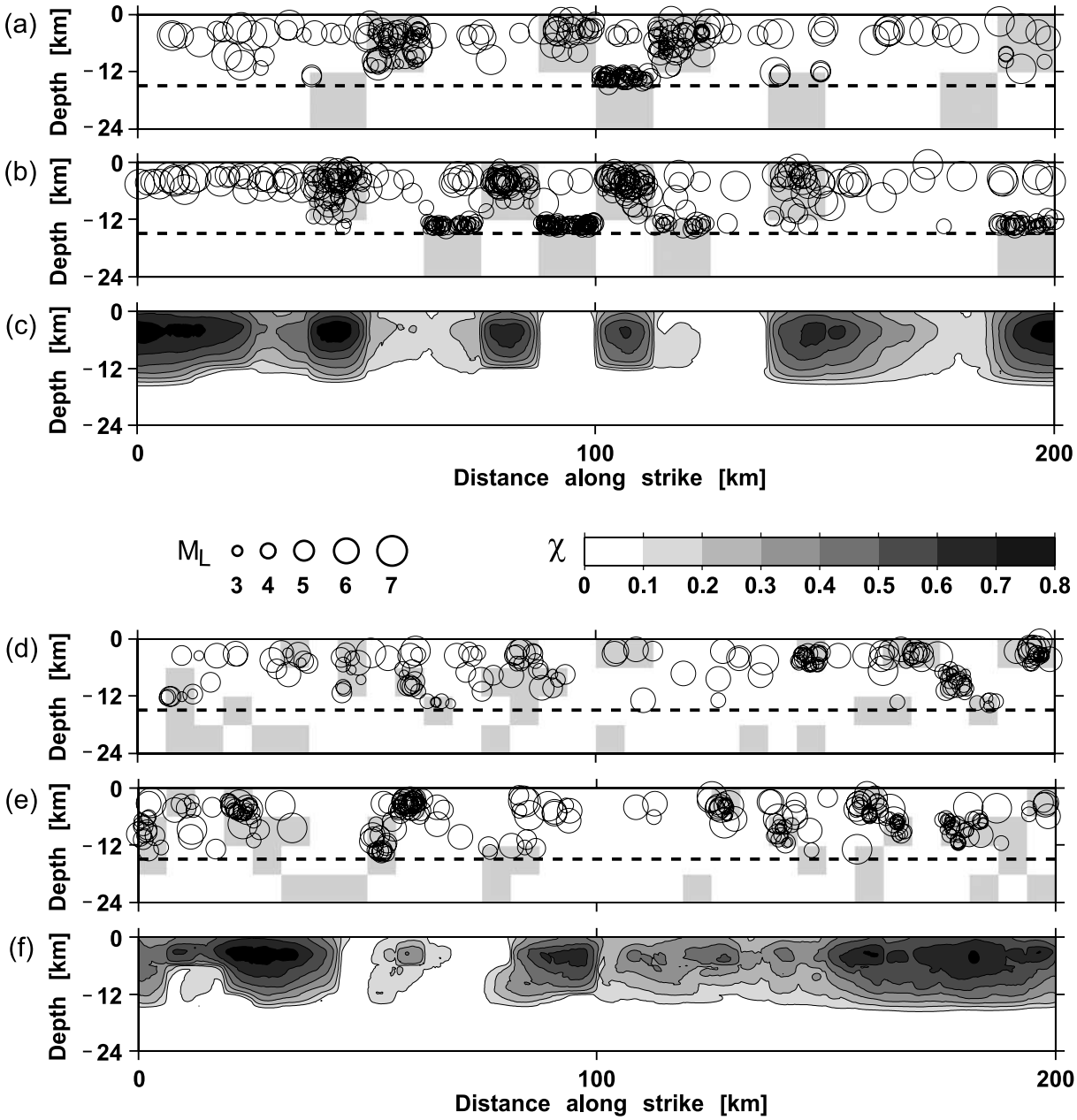

Figure 13. Spatial distribution of hypocenters for two P2 models (16 × 2 patches), (a) MP5 and (b) MP6 and two P3 models (32 × 4 patches), (d) MP7 and (e) MP8. Grey patches denote regions where L is small, i.e., $L \in \log_{10}([L_{\min}, L_{\min} + (L_{\max} - L_{\min})/4])$. This choice is motivated by histograms showing the number of events as a function of L at the hypocenter (e.g., Figure 10, left). Most events nucleate in the lower fourth of the L interval. (c) and (f) The spatial distribution of the coupling coefficient, χ, corresponds to seismicity displayed in Figures 13b and 13e, respectively. Dashed line in Figures 13a, 13b, 13d, and 13e marks lower bound of the seismogenic zone defined by $a < b$.

shock intervals (not shown) in response to heterogeneous L distributions (P3, P4, Figures 9c and 9d) verify the general trend of an increasing ε prior to large earthquakes. Models with more homogeneous pattern (especially P1) show no accelerated moment release. There, we could speak of 'quiescence' preceding large events. This demonstrates that our model allows to look at features like accelerated moment release. We leave, however, the discussion of detailed functional dependence of accelerating energy release for additional studies of future work.

[47] The results discussed so far are not controlled by specific assignments of $L \in \log_{10}([L_{\min}, L_{\max}])$ to specific chessboard pattern (8 × 1–64 × 8) but on the degree of heterogeneity. Figure 13 illustrates this qualitatively, where hypocenters at their actual location on the fault plane are plotted for two realizations of each patch pattern (P2: MP5, MP6; P3: MP7, MP8 in Table 2). For clarity, we highlight only patches where $L \in \log_{10}([L_{\min}, L_{\min} + (L_{\max} - L_{\min})/4])$, since most events nucleate in this interval (see histograms in Figures 10 and 12). The seismicity in Figures 13a, 13b,

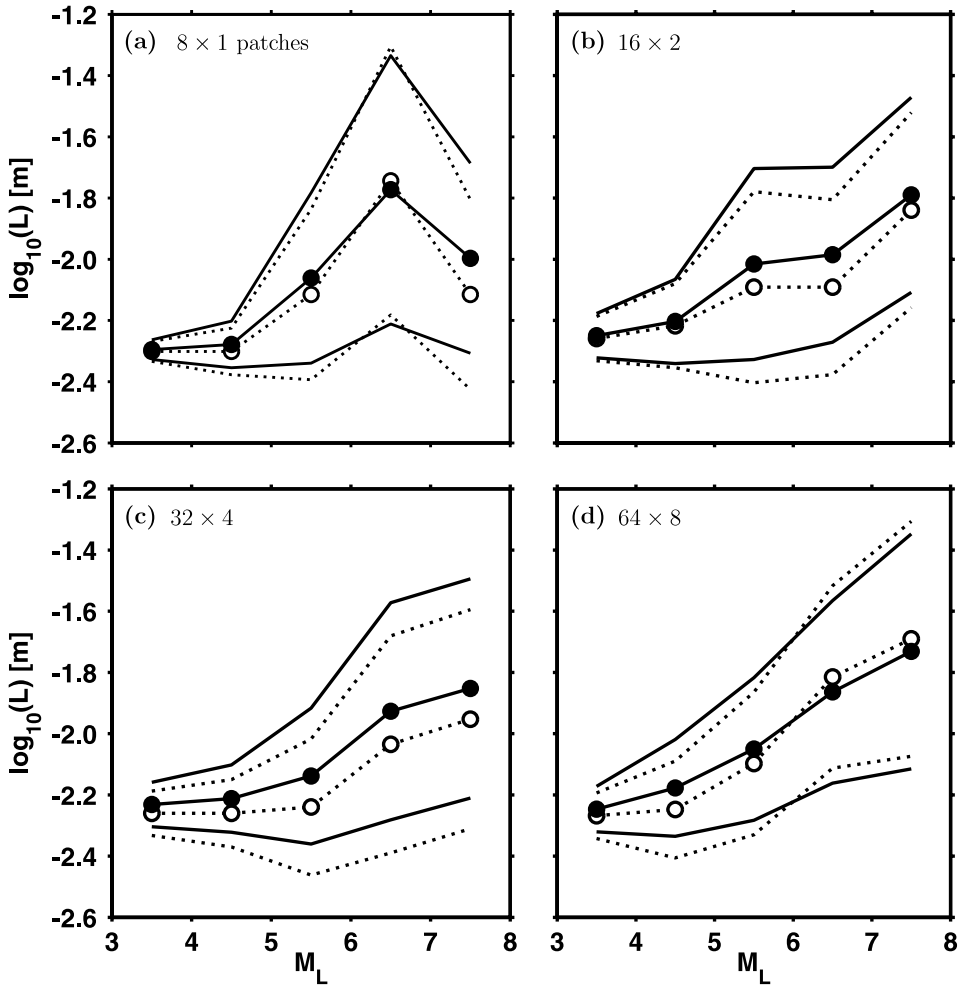

Figure 14. Mean (solid circles) and median (open circles) $\log_{10}(L)$ value at hypocenter locations as a function of magnitude range plus/minus one standard deviation (mean, solid line; median, dotted line). The data indicate that small earthquakes tend to nucleate at sites of relatively small L but large events have their hypocenters in regions of large L. Data sets from two simulations of each model class (P1–P4, Figures 14a–14d) have been stacked. Total number of earthquakes used are (a) 542, (b) 622, (c) 426, and (d) 853. In the magnitude range, data point at, e.g., $M_L = 4.5$, contains events with $4 \leq M_L < 5$.

13d, and 13e appears to reflect the property distributions. Hypocenters occur over the entire fault plane but most of them are in regions of small L. Figures 13a and 13b display a strong clustering above the $a - b$ induced velocity weakening to strengthening transition at $z = -15$ km in regions where L is small. For large-scale heterogeneities, seismic coupling χ shows a strong dependence of seismic stress release on the underlying value of the critical slip distance. Figure 13c displays strong coupling where L is small. The first 25 km and last 10 km along strike show large seismic coupling although there L is not taken from the lower fourth of the interval. Moderate size and large earthquakes nucleating there contribute significantly to seismic stress release. Small earthquakes nucleating below $z = -12$ km have no influence on the χ distribution. The spatial distribution of χ for a fault with small-scale heterogeneities (Figure 13f) reflects the corresponding L distribution less strong (Figure 13e, see Figure 9c). Regions of high activity do not necessarily lead to a strong coupling (e.g., cluster in Figure 13e at $x = 60$ km).

[48] Figure 14 plots the mean (and median) $\log_{10}(L)$ at hypocenter locations as a function of magnitude range. The data are compiled from two simulations of patch discretization (P1–P4) and are stacked to one graph for clarity. We identify a trend, which becomes more significant the finer the discretization of the L distribution is, that small earthquakes tend to nucleate at sites of relatively small L, whereas large events have their hypocenters in regions of large L. We conclude that the size of nucleation zone (h^*) tend to differ between small and large events, because $h^* \propto L$ (equation (7)) at depth sections where σ_e, a and b are constant (-2.5 km $> z > -14$ km). A likely interpretation of this result is that the growth of unstable small regions can be arrested by small scale unfavorable θ states in their vicinity. On the other hand, accelerating large regions tend to continue to grow into large slip events despite small-scale fluctuations in θ. The results are thus compatible with an overall positive correlation between the size of the nucleation zone and the final size of the earthquake. The statistical relevance of the correlation can be questioned, since we analyze

only two models for each degree of heterogeneity. However, the results are likely to be representative since each of the two realizations shows the same trend.

[49] Figure 15 illustrates that even high contrasts at patch boundaries of L patterns (P1–P4) do not cause discontinuities in slip maps. This reflects the smooth character of the underlying continuous solution. The modeled slip distributions from large events ($M_L > 6$) are comparable to slip distributions compiled from real earthquakes (http://www.seismo.ethz.ch/srcmod). The visual similarity validates the applicability of the chosen approach to study mechanisms responsible for observed features of natural seismicity. Future work will focus on the evaluation of statistical properties of synthetic slip maps to quantify the similarity to natural seismic events [*Mai and Beroza*, 2000].

6. Hybrid Model

[50] A third type of 2-D L distributions combines the approaches used in previous sections. In particular, we link the depth-dependent L profile from section 4 with the chessboard pattern from section 5. Therefore the general structure of a shear zone with depth (section 3) in addition to geometrical heterogeneity along the fault (section 5) are both treated. Figure 16a (left) shows a heterogeneous L distribution along strike at seismogenic depth (-3 km $> z > -15$ km) with $L \in \log_{10}([0.005, 0.1])$ m. Above and below this zone L is homogeneous along strike and increases to L_{top}, L_{btm}, with $L_{min} = 0.005$ m and $\alpha = 10^3$ (MH1 in Table 3). The results shown are obtained with an $a - b$ profile that stabilizes the fault at depth but is velocity weakening in the topmost part of the fault (Figure 3a, profile 2). Note that L influences the response only at $z > -18$ km. At greater depths $b = 0$ and hence L cannot control the evolution of μ anymore (see Figure 1 and equation (2)). The corresponding hypocenter locations (Figure 16b) show an even stronger clustering than those for the simpler chessboard models (Figures 13d and 13e). The hypocenter locations as a function of L follow the same trend as those generated by models without the particular L depth dependence (Figure 16c). Most events nucleate at sites where L is relatively small. In contrast to previous simulations, all events nucleate in regions where L is smaller than 0.02 m (inferred from Figure 16c). The FS statistics have a relatively large "b value" representing a high ratio of small to large earthquakes. The simulated maximum and mean magnitude of $M_L = 6.8$ and $M_L = 4.7$, respectively, are significantly smaller than those obtained with simpler chessboard patterns.

[51] A number of evidence imply an increase in complex seismic response: (1) A higher rate ($r = 1.05$ events/year); (2) the stress function AS exhibits a less pronounced saw-tooth-like temporal evolution, with moderate oscillations around a relatively high temporal stress average (4.6 MPa $>\sim$ 4.3 MPa, Figures 16d and 11a–11c); (3) the stress fluctuations are persistent in time due to high seismic activity (deviations from a background level are relatively small (SD, Figure 16e)); and (4) the seismicity evolution reveals a less distinct differentiation between quiescence and seismically active periods. In general, magnitudes are smaller than $M_L = 6.5$.

[52] Although the seismic productivity is somewhat higher than in the models without depth-dependent L, the seismic coupling is significantly smaller, $\chi = 0.01$. Most of the events are small and only a few larger slip instabilities occur, which is reflected in the relatively large slope of the FS statistics. We performed an additional simulation employing the same L pattern with $a - b = -0.004 = \text{const}$ (MH2 in Table 3), but the resulting characteristics of model seismicity remain unchanged. Thus the solution is less sensitive to the $a - b$ profile when the applied L distribution increases below the seismogenic zone, although for profile 2 in Figure 3a L does not influence the response at $z < -18$ km.

[53] Figure 16 (right) displays the response for hybrid model MH3. The 12 km deep seismogenic depth section is divided into 64×4 patches, $L \in \log_{10}([0.005, 0.1\text{ m}])$. As in MH1, we use $\alpha = 10^3$ to determine L_{top}, L_{btm} (Figure 16a). We keep $a - b$ constant, as in MH2. The hypocenter locations are highly localized in regions where $L < 0.008$ m. The map view of Figure 16b and the histogram in Figure 16c reveal this strong clustering. Thus increased geometrical complexity of the critical slip distance leads to less distributed nucleation zones. Moreover, the slope of generated FS statistics is comparable to the mean strike-slip fault value of -0.75, although the largest earthquake has a magnitude of only $M_L = 5.8$. The stress functions AS and SD (Figures 16d and 16e) can be compared to those generated by the discrete model FC of *Ben-Zion et al.* [2003a], developing small-amplitude fluctuations around the temporal average. Finally, the temporal seismicity evolution (Figure 16f) shows that the model produces a continuous stream of small earthquakes around $M_L = 4$. There is no periodicity in seismicity evolution, i.e., the fault slips in a relatively stable fashion without generating large events. The seismicity pattern prior to $t = 400$ years appears to be slightly different compared to $t > 400$ years illustrating the systems' departure from the influence of initial conditions.

[54] Whereas the differences between the property distributions P3, P4 and MH1, MH3 are related (doubling the number of L patches), the differences of responses are more pronounced between MH1 and MH3. MH1 and MH2 generate statistical similar results (see Table 3). The fundamental change from MH1 to MH3 is primarily due to the increase in structural heterogeneity and only secondary related to changes in $a - b$ at depth.

7. Discussion and Conclusions

[55] Previous works have shown that fault models belonging to the continuum class with relatively homogeneous frictional properties [*Tse and Rice*, 1986; *Rice*, 1993; *Ben-Zion and Rice*, 1997; *Lapusta et al.*, 2000] do not produce in general slip events over a broad range of magnitudes. *Cochard and Madariaga* [1996], *Nielsen et al.* [2000] and *Shaw and Rice* [2000] confirmed that generation of slip complexity on a homogeneous fault requires special choices of constitutive and model parameters. As summarized by *Ben-Zion* [2001], those choices involve several properties that are not general characteristics of available lab data, including very large strength drop behind the rupture front followed by rapid dynamic healing, constitutive laws with several weakening mechanisms that

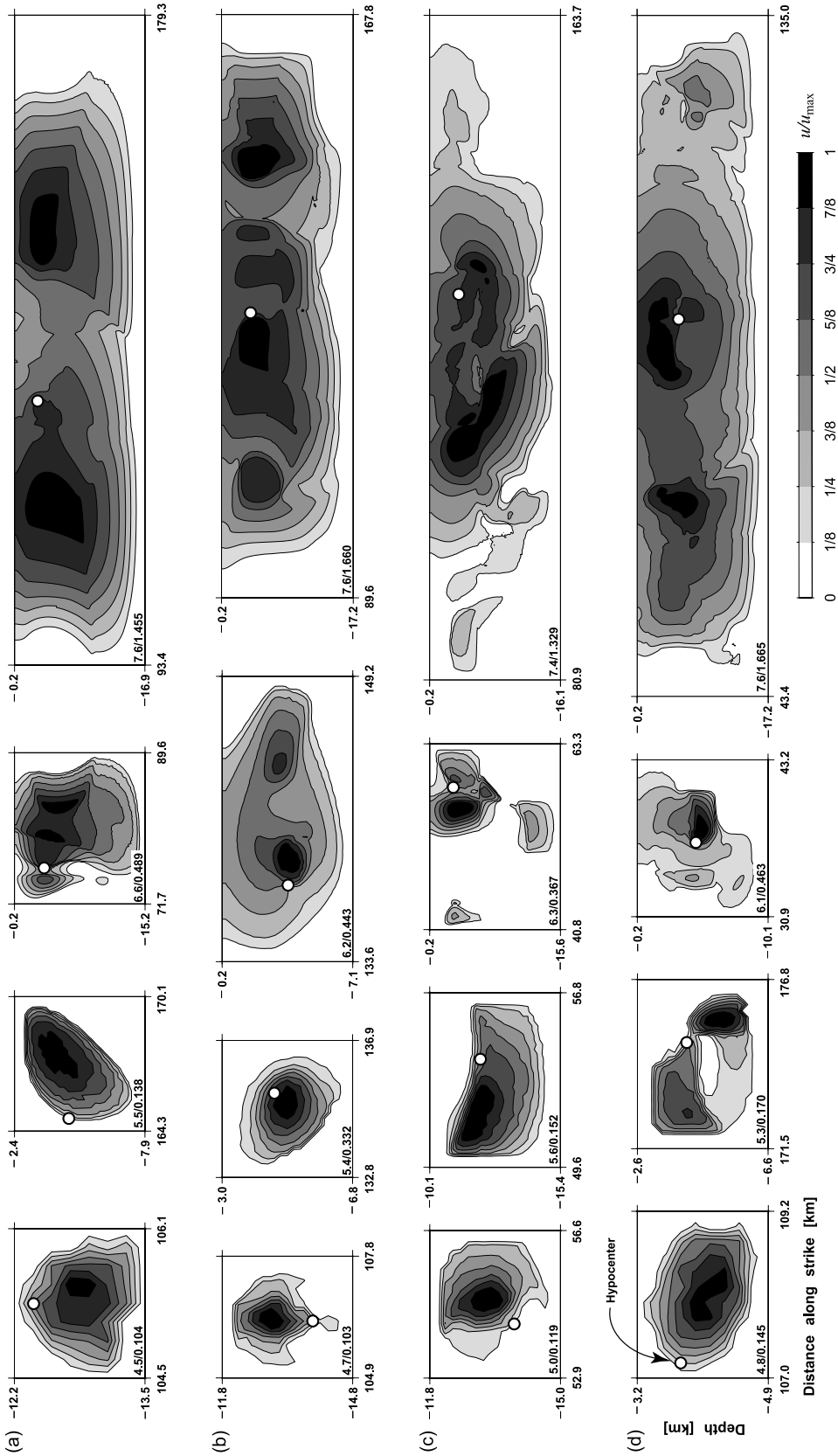

Figure 15. Examples of final slip distributions. Events with four different magnitudes are taken from four simulations corresponding to L distributions in Figures 9a–9d. Magnitude, M_L, and maximum slip, u_{max}, are given in lower left corner of each slip map. Grey intensity is scaled to u_{max} of each single event. White dots denote hypocenters. The distances along strike and depth correspond to the actual position on the 200 km × 24 km fault.

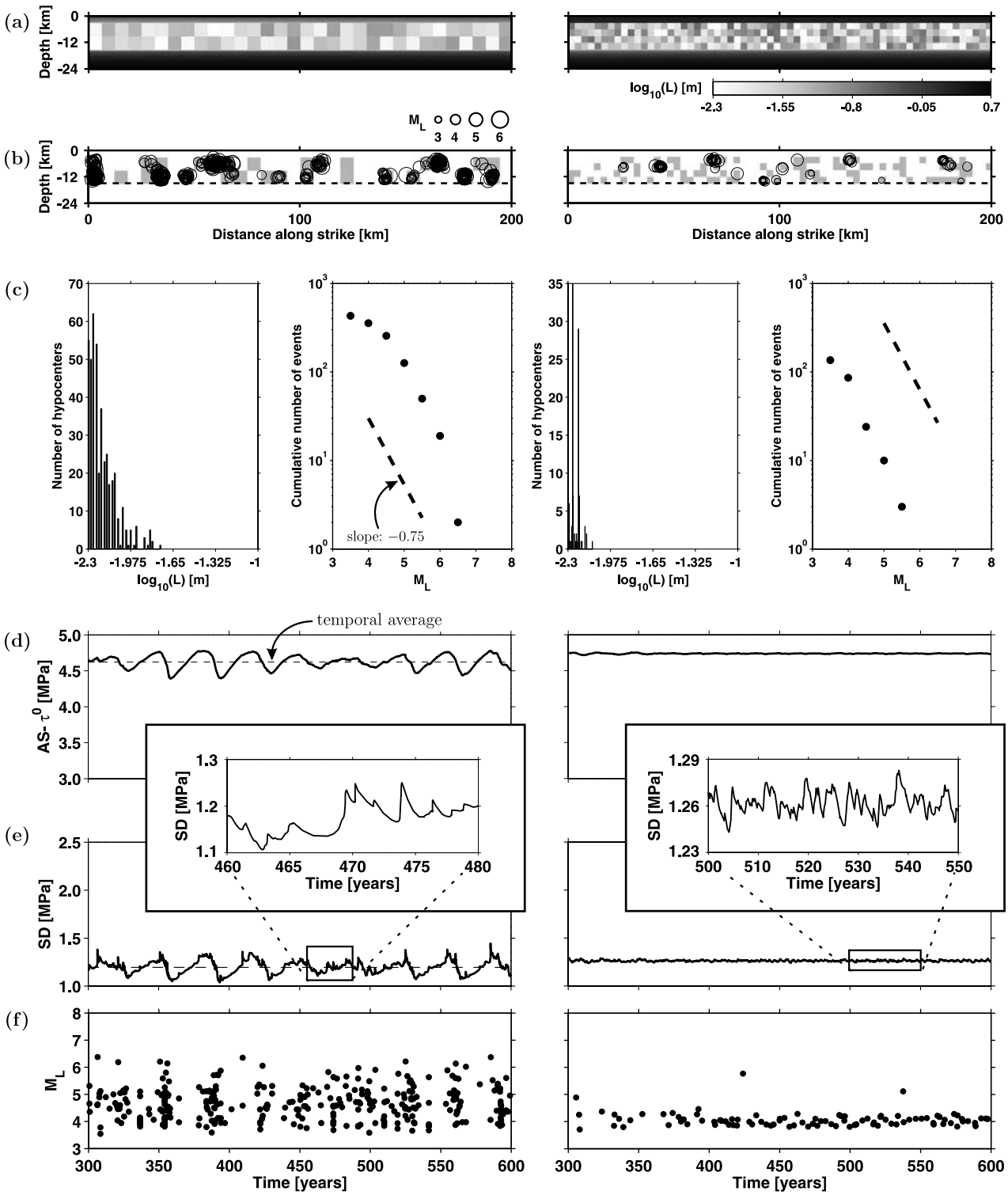

Figure 16. (left) Response to model MH1, (a) 2-D depth-dependent L distribution, 32 $\times$ 2 patches between $z = -3$ and $z = -15$ km; $a - b$ profile 2 of Figure 3a. (right) Response to model MH3, 2-D depth-dependent L distribution (Figure 16a), 64 $\times$ 4 patches between $z = -3$ and $z = -15$ km; $a - b = -0.004$ = const. For both models, $L_{\min} = 0.005$ m, $\alpha = 10^3$. (b) Spatial distribution of hypocenters. (c) Hypocenter location as a function of L and resulting FS statistics. (d) Average stress AS. (e) Standard deviation of stress, SD, in the top 15 km. (f) Temporal seismicity evolution.

Table 3. Overview of Models Using Hybrid L Distributions[a]

Model Name	L Pattern	L_{min}, m	α	$a - b$	Number of Patches	X_{length}, km	Z_{depth}, km	nx	nz	h/h^*	Response Type	r	χ	Figure
MH1	hybrid	0.005	10^3	profile 2	32×2	200	24	1024	256	0.4	pattern	1.05	0.01	16
MH2	hybrid	0.005	10^3	const	32×2	200	24	1024	256	0.4	pattern	0.84	0.01	–
MH3	hybrid	0.005	10^3	const	64×4	200	24	1024	256	0.4	pattern	0.37	<0.01	16

[a]Profile 2 for $a - b$ refers to Figure 3a.

are tuned to produce separate event populations in different size ranges, and/or saturation of the growth of stress concentrations with rupture size. *Lapusta et al.* [2000] simulated small events prior to large ones in a continuum model with RS friction, but those are a direct consequence of the $a - b$ transition zone at $z = -15$ km (see Lapusta et al.'s Figure 6). *Hirose and Hirahara* [2002] generated complex slip behavior by placing in a 3-D continuous subduction zone model asperities that produce slip heterogeneities. *Liu and Rice* [2005] demonstrated with a 3-D quasi-dynamic subduction model in the continuum limit that small variations in a and b along strike can produce nonuniform spatiotemporal slip response. This indicates, in agreement with previous works [*Ben-Zion and Rice*, 1995; *Rice and Ben-Zion*, 1996], that some degree of spatial heterogeneity in continuum models is required to produce spatiotemporal complex seismic behavior.

[56] In contrast to the above continuum models, a wide variety of discrete models, with built-in strong heterogeneities associated with the model discreteness, were shown to produce generic slip complexities over broad ranges of scales [*Burridge and Knopoff*, 1967; *Langer et al.*, 1996; *Carlson and Langer*, 1989a, 1989b; *Carlson et al.*, 1991; *Bak et al.*, 1987, 1988; *Bak and Tang*, 1989; *Ito and Matsuzaki*, 1990; *Lomnitz-Adler*, 1993; *Ben-Zion*, 1996; *Zöller et al.*, 2005b, 2005c; *Dahmen et al.*, 1998]. It has been argued that fault segments that are geometrically discontinuous may be represented approximately by the discrete numerical elements [*Ben-Zion and Rice*, 1993; *Rice and Ben-Zion*, 1996; *Ben-Zion*, 2001]. The inherent discreteness in those models allows the elements to fail independently in small earthquakes, while cascades of failures of a number of elements produce moderate and large events. *Ben-Zion* [1996], *Ben-Zion et al.* [2003a], and *Zöller et al.* [2005c] suggested that the degree of fault heterogeneities may act as a tuning parameter for the fault dynamics.

[57] In this study we developed a model that represents fault zone heterogeneity by variations of the critical slip distance L of rate- and state-dependent friction [*Dieterich*, 1979; *Ruina*, 1983; *Rice*, 1993; *Ben-Zion*, 2003], and a procedure for extracting seismic catalog from continuous fault slip data. We explored basic effects of structural irregularities and topology of fault surfaces by performing systematic simulations of a quasi-dynamic continuum model of a 2-D strike-slip fault with heterogeneous distributions of L. The incorporation of spatially heterogeneous distribution of the L parameter allows us to produce realistic slip and stress complexities within the continuum class of models. This bridges the gap between previous works associated with the smooth continuum and inherently discrete models. The results support previous conclusions on the dominant roles of fault heterogeneities on the simulated response, and the suggestion that they may act as a tuning parameter of the dynamics. We note that stronger forms of heterogeneities associated with fault discreteness may be needed [*Zöller et al.*, 2005a, 2005b] to produce additional realistic features of seismicity in a single fault zone such as aftershocks and accelerated seismic release. A full treatment of such features requires a modeling approach that accounts for a regional response with many interacting faults [e.g., *Ben-Zion and Lyakhovsky*, 2002, 2006].

[58] The cases examined in this work involve three sets of realizations: (1) homogeneous L distributions along strike but realistic depth variations constrained by shear zone structure; (2) chessboard-like 2-D pattern with different length scales of irregularity; and (3) a hybrid approach combining the first two implementation types. We observe the following trends and response characteristics:

[59] 1. Our calculated response for a standard model with frictional properties corresponding to fairly homogeneous faults agrees generally with previous studies. Here $a - b$ follows a depth dependent profile and the critical slip distance L is constant throughout the plane. We generated several models where we keep $a - b < 0 =$ const (unstable), while using a depth-dependent L profile. This parameterization was shown to produce similar space-time stick-slip pattern to that simulated in the past with variable $a - b$ profiles. For $\alpha \geq 10^2$, a scaling factor to determine L_{btm} and L_{top}, the model generates irregular spatiotemporal slip patterns. Although details are controlled by specific model dimensions and chosen discretizations of the numerical implementation, the general features are robust (see Table 1).

[60] 2. A fault with heterogeneous 2-D L distributions produces a broad range of event sizes. Regions with small L values are more likely to have a hypocenter. The seismicity rate increases when the fault is divided into smaller patches. On fairly homogeneous faults, large-scale average stress fluctuations are significant. Relatively heterogeneous cases produce pronounced small-scale stress fluctuations (see Table 2). We observe a trend of an increasing seismic strain release prior to large earthquakes, in general agreement with the critical point theory. For fairly homogeneous faults, the spatial seismic coupling correlates with regions where L is relatively small. This correspondence is less pronounced for geometrically disordered surfaces. Example maps of final slip of simulated events show properties similar to those observed of natural strike-slip earthquakes.

[61] 3. The hybrid approach affirms the stabilizing effect of large L values at depth, since models with either depth-dependent or constant $a - b$ distributions produce qualitatively comparable results. However, example simulation of a fairly heterogeneous fault produces different statistical properties of the seismicity than less heterogeneous realizations (see Table 3).

[62] The mean L at the hypocenter and hence the size of the nucleation zone of large earthquakes differ from those of

small and moderate events for all cases studied (Figure 14). For more homogeneous faults the signal is less monotonous, but nevertheless reveals a trend that nucleation size correlates with the event size. Although the relation between the nucleation size and corresponding seismic nucleation phases can depend on additional factors, these results may serve as a contribution to the debate on whether small and large earthquakes show comparable or different initial seismic stages. As *Lapusta and Rice* [2003] demonstrated, small and large model events on a smooth fault plane can exhibit the same nucleation phase. In contrast, our simulations with heterogeneous faults suggest that small and larger events are associated, statistically, with different nucleation sizes. *Iio* [1995], *Ellsworth and Beroza* [1995], and *Beroza and Ellsworth* [1996] argued that the seismic nucleation phases of earthquakes scale with the size of the events. However, other studies showed opposite or no such scaling [*Anderson and Chen*, 1995; *Mori and Kanamori*, 1996]. Although we do not compute these phases in detail, the increase toward larger L values at hypocenters of large events suggests a statistical scaling between the nucleation phases and the final size of an event. Maps that show spatially averaged sizes of nucleation zones may provide additional information on hypocenter locations (as shown in Figures 13a, 13b, 13d, and 13e). However, this is beyond the scope of the current investigation and is left for future work.

[63] The simulated slip maps (Figure 15) provide an opportunity to compare their statistical properties, such as hypocenter location with respect to high-slip regions [*Mai et al.*, 2005], to those of past recorded earthquakes compiled by P. M. Mai (A database of finite source rupture models, 2004, available at http://www.seismo.ethz.ch/srcmod). Systematic comparisons between observed and simulated slip histories, combined with comparisons of observed and simulated earthquake catalogs, may be used to invert for the underlying fault properties such as L distributions along given fault sections. This can lead to an improved understanding of the physical features that are responsible for various aspects of observed earthquake patterns. Future work will focus on effects generated by more realistic 2-D L distributions with statistical properties compatible with observations associated with natural fault zones at different evolutionary stages. The generated slip maps and other simulated results may serve as a starting point for estimating ground motion and probabilistic seismic hazard associated with various faults.

[64] **Acknowledgments.** We thank E. Hairer for numerous comments on handling and improving stability and performance of the numerical integrator and J. R. Rice and Y. Liu for the FFT algorithm for shear stress redistribution. N. Lapusta gave useful comments on the effect of initial conditions. W. P. Petersen, A. Bongulielmi, T. Racic, D. Schorlemmer, and J. Woessner provided computational assistance. The work was sponsored by EC-Project RELIEF (EVG1-CT-2002-00069) and the Southern California Earthquake Center (based on NSF cooperative agreement EAR-8920136 and U.S. Geological Survey cooperative agreement 14-08-0001-A0899). The manuscript benefited from useful comments by H. Perfettini, an anonymous referee, and Associate Editor S. Steacy.

References

Anderson, J., and Q. Chen (1995), Beginnings of earthquakes in the Mexican subduction zone on strong-motion accelerograms, *Bull. Seismol. Soc. Am.*, *85*, 1107–1116.

Bak, P., and C. Tang (1989), Earthquakes as a self-organized critical phenomenon, *J. Geophys. Res.*, *94*, 15,635–15,637.

Bak, P., C. Tang, and K. Wiesenfeld (1987), Self-organized criticality: An explanation of 1/f noise, *Phys. Rev. Lett.*, *59*(4), 381–384.

Bak, P., C. Tang, and K. Wiesenfeld (1988), Self-organized criticality, *Phys. Rev. A*, *38*(1), 364–374.

Ben-Zion, Y. (1996), Stress, slip, and earthquakes in models of complex single-fault systems incorporating brittle and creep deformations, *J. Geophys. Res.*, *101*, 5677–5706.

Ben-Zion, Y. (2001), Dynamic rupture in recent models of earthquake faults, *J. Mech. Phys. Solids*, *49*, 2209–2244.

Ben-Zion, Y. (2003), Key formulas in earthquake seismology, in *International Handbook of Earthquake and Engeneering Seismology, Part B*, Appendix 2, edited by W. H. Lee et al., pp. 1857–1875, Elsevier, New York.

Ben-Zion, Y., and V. Lyakhovsky (2002), Accelerating seismic release and related aspects of seismicity patterns on earthquake faults, *Pure Appl. Geophys.*, *159*, 2358–2412.

Ben-Zion, Y., and V. Lyakhovsky (2006), Analysis of aftershocks in a lithospheric model with seismogenic zone governed by damage rheology, *Geophys. J. Int.*, *164*, doi:10.111/j.1365-246X.2006.02878.x.

Ben-Zion, Y., and J. R. Rice (1993), Earthquake failure sequences along a cellular fault zone in a three-dimensional elastic solid containing asperity and nonasperity regions, *J. Geophys. Res.*, *98*, 14,109–14,131.

Ben-Zion, Y., and J. R. Rice (1995), Slip patterns and earthquake populations along different classes of faults in elastic solid, *J. Geophys. Res.*, *100*, 12,959–12,983.

Ben-Zion, Y., and J. R. Rice (1997), Dynamic simulations of slip on a smooth fault in an elastic solid, *J. Geophys. Res.*, *102*, 17,771–17,784.

Ben-Zion, Y., and C. G. Sammis (2003), Characterization of fault zones, *Pure Appl. Geophys.*, *160*, 677–715.

Ben-Zion, Y., and L. Zhu (2002), Potency-magnitude scaling relations for southern California earthquakes with $1.0 < M_L < 7.0$, *Geophys. J. Int.*, *148*, F1–F5.

Ben-Zion, Y., M. Eneva, and Y. Liu (2003a), Large earthquake cycles and intermittent criticality on heterogeneous faults due to evolving stress and seismicity, *J. Geophys. Res.*, *108*(B6), 2307, doi:10.1029/2002JB002121.

Ben-Zion, Y., Z. Peng, D. Okaya, L. Seeber, J. G. Armbruster, N. Ozer, A. J. Michael, S. Baris, and M. Aktar (2003b), A shallow fault zone structure illuminated by trapped waves in the Karadere-Duzce branch of the North Anatolian Fault, western Turkey, *Geophys. J. Int.*, *152*, 699–717.

Beroza, G. C., and W. L. Ellsworth (1996), Properties of the seismic nucleation phase, *Tectonophysics*, *261*, 209–227.

Blanpied, M. L., D. A. Lockner, and J. D. Byerlee (1991), Fault stability inferred from granite sliding experiments at hydrothermal conditions, *Geophys. Res. Lett.*, *18*(4), 609–612.

Bowman, D. D., G. Ouillon, C. G. Sammis, A. Sornette, and D. Sornette (1998), An observational test on the critical earthquake concept, *J. Geophys. Res.*, *103*, 24,359–24,372.

Burridge, R., and L. Knopoff (1967), Model and theoretical seismicity, *Bull. Seismol. Soc. Am.*, *57*, 341–371.

Carlson, J. M., and J. S. Langer (1989a), Properties of earthquakes generated by fault dynamics, *Phys. Rev. Lett.*, *62*(22), 2632–2635.

Carlson, J. M., and J. S. Langer (1989b), Mechanical model of an earthquake fault, *Phys. Rev. A*, *40*(11), 6470–6484.

Carlson, J. M., J. S. Langer, B. E. Shaw, and C. Tang (1991), Intrinsic properties of a Burridge-Knopoff model of an earthquake fault, *Phys. Rev. A*, *44*(2), 884–897.

Chester, F. M., and J. S. Chester (1998), Ultracataclasite structure and friction processes of the Punchbowl Fault, San Andreas System, California, *Tectonophysics*, *295*, 199–221.

Chinnery, M. (1963), The stress changes that accompany strike-slip faulting, *Bull. Seismol. Soc. Am.*, *53*, 921–932.

Cochard, A., and R. Madariaga (1996), Complexity of seismicity due to highly rate-dependent friction, *J. Geophys. Res.*, *101*, 25,321–25,336.

Dahmen, K., D. Ertas, and Y. Ben-Zion (1998), Gutenberg-Richter and characteristic earthquake behavior in simple mean field models of heterogeneous faults, *Phys. Rev. E*, *58*, 1494–1501.

Dieterich, J. H. (1979), Modeling of rock friction: 1. Experimental results and constitutive equations, *J. Geophy. Res.*, *84*, 2161–2168.

Dieterich, J. H. (1994), A constitutive law for rate of earthquake production and its application to earthquake clustering, *J. Geophys. Res.*, *99*, 2601–2618.

Dieterich, J. H., V. Cayol, and P. Okubo (2000), The use of earthquake rate changes as a stress meter at Kilauea volcano, *Nature*, *408*, 457–460.

Ellsworth, W. L., and G. C. Beroza (1995), Seismic evidence for an earthquake nucleation phase, *Science*, *268*, 851–855.

Frohlich, C., and S. D. Davis (1993), Teleseismic *b* values: Or, much ado about 1.0, *J. Geophys. Res.*, *98*, 631–644.

Hairer, E., S. P. Norsett, and G. Wanner (Eds.) (1993), *Solving Ordinary Differential Equations: I. Nonstiff Problems*, 2nd ed., 523 pp., Springer, New York.
Hirose, H., and K. Hirahara (2002), A model for complex slip behavior on a large asperity at subduction zones, *Geophys. Res. Lett.*, *29*(22), 2068, doi:10.1029/2002GL015825.
Iio, Y. (1995), Observation of the slow initial phase of microearthquakes: Implications for earthquake nucleation and propagation, *J. Geophys. Res.*, *100*, 15,333–15,349.
Ito, K., and M. Matsuzaki (1990), Earthquakes as self-organized critical phenomena, *J. Geophys. Res.*, *95*, 6853–6860.
Jaumé, S. C., and L. R. Sykes (1999), Evolving towards a critical point: A review of accelerating seismic moment/energy release prior to large and great earthquakes, *Pure Appl. Geophys.*, *155*, 279–306.
Kato, N., and T. Hirasawa (1999), Nonuniform and unsteady sliding of a plate boundary in a great earthquake cycle: A numerical simulation using a laboratory-derived friction law, *Pure Appl. Geophys.*, *155*, 93–118.
Kostrov, B. (1974), Seismic moment and energy of earthquakes, and seismic flow of rock, *Izv. Acad. Sci. USSR, Phys. Solid Earth*, Engl. Transl., *1*, 23–40.
Langer, J. S., J. M. Carlson, C. R. Myers, and B. E. Shaw (1996), Slip complexity in dynamic models of earthquake faults, *Proc. Natl. Acad. Sci. U.S.A.*, *93*, 3825–3829.
Lapusta, N., and J. R. Rice (2003), Nucleation and early seismic propagation of small and large events in a crustal earthquake model, *J. Geophys. Res.*, *108*(B4), 2205, doi:10.1029/2001JB000793.
Lapusta, N., J. R. Rice, Y. Ben-Zion, and G. Zheng (2000), Elastodynamic analysis for slow tectonic loading with spontaneous rupture episodes on faults with rate- and state-dependent friction, *J. Geophys. Res.*, *105*, 23,765–23,789.
Liu, Y., and J. R. Rice (2005), Aseismic slip transients emerge spontaneously in three-dimensional rate and state modeling of subduction earthquake sequences, *J. Geophys. Res.*, *110*, B08307, doi:10.1029/2004JB003424.
Lomnitz-Adler, J. (1993), Automaton models of seismic fracture: Constraints imposed by the magnitude-frequency relation, *J. Geophys. Res.*, *98*, 17,745–17,756.
Lyakhovsky, V., Y. Ben-Zion, and A. Agnon (2001), Earthquake cycle, fault zones, and seismicity patterns in a rheologically layered lithosphere, *J. Geophys. Res.*, *106*, 4103–4120.
Mai, P. M., and G. Beroza (2000), Source scaling properties from finite-fault-rupture models, *Bull. Seismol. Soc. Am.*, *90*(3), 604–615.
Mai, P. M., P. Spudich, and J. Boatwright (2005), Hypocenter locations in finite-source rupture models, *Bull. Seismol. Soc. Am.*, *95*(3), 965–980.
Marone, C. (1998), Laboratory-derived friction laws and their application to seismic faulting, *Annu. Rev. Earth Planet. Sci.*, *26*, 643–696.
Miller, S. A., Y. Ben-Zion, and J.-P. Burg (1999), A three-dimensional fluid-controlled earthquake model: Behavior and implications, *J. Geophys. Res.*, *104*, 10,621–10,638.
Mora, P., and D. Place (2002), Stress correlation function evolution in lattice solid elasto-dynamic models of shear and fracture zones and earthquake prediction, *Pure Appl. Geophys.*, *159*, 2413–2427.
Mori, J., and H. Kanamori (1996), Initial rupture of earthquakes in the 1995 Ridgecrest, California sequence, *Geophys. Res. Lett.*, *23*, 2437–2440.
Nielsen, S. B., J. M. Carlson, and K. B. Olsen (2000), Influence of friction and fault geometry on earthquake rupture, *J. Geophys. Res.*, *105*, 6069–6088.
Ohnaka, M. (2003), A constitutive scaling law and a unified comprehension for frictional slip failure, shear fracture of intact rock, and earthquake rupture, *J. Geophys. Res.*, *108*(B2), 2080, doi:10.1029/2000JB000123.
Parsons, T., S. Toda, R. S. Stein, A. Barka, and J. H. Dieterich (2000), Heightened odds of large earthquakes near Istanbul: An interaction-based probability calculation, *Science*, *288*, 661–665.
Perfettini, H., and M. Campillo (2003), On the scaling of the slip weakening rate of heterogeneous faults, *J. Geophys. Res.*, *108*(B9), 2410, doi:10.1029/2002JB001969.
Perfettini, H., J. Schmittbuhl, and A. Cochard (2003), Shear and normalload perturbations on a 2D continuous fault: 1. Static triggering, *J. Geophys. Res.*, *108*(B9), 2408, doi:10.1029/2002JB001804.
Rice, J. R. (1993), Spatiotemporal complexity of slip on a fault, *J. Geophys. Res.*, *98*, 9885–9907.
Rice, J. R., and Y. Ben-Zion (1996), Slip complexity in earthquake fault models, *Proc. Natl. Acad. Sci. U.S.A.*, *93*, 3811–3818.
Robinson, R., and R. Benites (1995), Synthetic seismicity models for multiple interacting faults, *J. Geophys. Res.*, *100*, 18,229–18,238.
Ruina, A. (1983), Slip instability and state variable friction laws, *J. Geophy. Res.*, *88*, 10,359–10,370.
Scholz, C. H. (1988), The brittle-plastic transition and the depth of seismic faulting, *Geol. Rundsch.*, *77*, 319–328.
Scholz, C. H. (Ed.) (2002), *The Mechanics of Earthquakes and Faulting*, 2nd ed., 471 pp., Cambridge Univ. Press, New York.
Shaw, B. E., and J. R. Rice (2000), Existence of continuum complexity in the elastodynamics of repeated fault ruptures, *J. Geophys. Res.*, *105*, 23,791–23,810.
Shibazaki, B., and Y. Iio (2003), On the physical mechanism of silent slip events along the deeper part of the seismogenic zone, *Geophys. Res. Lett.*, *30*(9), 1489, doi:10.1029/2003GL017047.
Sornette, D. (2002), Predictability of catastrophic events: Material rupture, earthquakes, turbulence, financial crashes, and human birth, *Proc. Natl. Acad. Sci. U.S.A.*, *99*, 2522–2529.
Sornette, D., and C. G. Sammis (1995), Complex critical exponent from renormalization group theory of earthquakes: Implications for earthquake predictions, *J. Phys. I*, *5*, 607–619.
Stein, R. S. (2003), Earthquake conversations, *Sci. Am.*, *288*, 72–79.
Stesky, R. M. (Ed.) (1975), The mechanical behavior of faulted rock at high temperature and pressure, Ph.D. thesis, Mass. Inst. of Technol., Cambridge.
Stirling, M. W., S. G. Wesnousky, and K. Shimazaki (1996), Fault trace complexity, cumulative slip, and the shape of the magnitude-frequency distribution for strike-slip faults: A global survey, *Geophys. J. Int.*, *124*, 833–868.
Stuart, W. D., and T. E. Tullis (1995), Fault model for preseismic deformation at Parkfield, California, *J. Geophys. Res.*, *100*, 24,079–24,099.
Sylvester, A. G. (1988), Strike-Slip Faults, *Geol. Soc. Am. Bull.*, *100*, 1666–1703.
Toda, S., R. S. Stein, and T. Sahiya (2002), Evidence from the AD 2000 Izu islands earthquake swarm that stressing rate governs seismicity, *Nature*, *419*, 58–61.
Tse, S. T., and J. R. Rice (1986), Crustal earthquake instability in relation to the depth variation of frictional slip properties, *J. Geophys. Res.*, *91*, 9452–9472.
Tullis, T. E. (1996), Rock friction and its implications for earthquake prediction examined via models of Parkfield earthquakes, *Proc. Natl. Acad. Sci. U.S.A.*, *93*, 3803–3810.
Wesnousky, S. G. (1988), Seismological and structural evolution of strike-slip faults, *Nature*, *335*, 340–343.
Wesnousky, S. G. (1994), The Gutenberg-Richter or characteristic earthquake distribution, Which is it?, *Bull. Seismol. Soc. Am.*, *84*(6), 1940–1959.
Zöller, G., and S. Hainzl (2002), A systematic spatiotemporal test of the critical point hypothesis for large earthquakes, *Geophys. Res. Lett.*, *29*(11), 1558, doi:10.1029/2002GL014856.
Zöller, G., S. Hainzl, Y. Ben-Zion, and M. Hohlschneider (2005a), Earthquake activity related to seismicity cycles in a model for a heterogeneous strike-slip fault, *Tectonophysics*, in press.
Zöller, G., S. Hainzl, M. Hohlschneider, and Y. Ben-Zion (2005b), Aftershocks resulting from creeping sections in a heterogeneous fault, *Geophys. Res. Lett.*, *32*, L03308, doi:10.1029/2004GL021871.
Zöller, G., M. Hohlschneider, and Y. Ben-Zion (2005c), The role of heterogeneities as a tuning parameter of earthquake dynamics, *Pure Appl. Geophys.*, *162*, 1027.1049, doi:10.1007/s00024-004-2660-9.

Y. Ben-Zion, Department of Earth Sciences, University of Southern California, Zumberge Hall, 3651 Trousdale Ave., Room 109, Los Angeles, CA 90089-0740, USA. (benzion@usc.edu)
G. Hillers and P. M. Mai, Institute of Geophysics, HPP P3, ETH Zürich, Schafmattstrasse 30, CH-8093 Zürich, Switzerland. (hillers@sed.ethz.ch)